Azimuthal Anisotropy of Particle Emission in Au+Au Collisions at RHIC-PHENIX

Masaya ONO

(Doctoral Program in Physics)

Submitted to the Graduate School of
Pure and Applied Sciences
in Partial Fulfillment of the Requirements
for the Degree of Master of Science
at the
University of Tsukuba

February 2002

Azimuthal Anisotropy of Particle Emission in Au+Au Collisions at RHIC-PHENIX

Masaya ONO

(Doctoral Program in Physics)

Advised by

Yasuo MIAKE

_____

ShinIchi ESUMI

_____

Submitted to the Graduate School of
Pure and Applied Sciences
in Partial Fulfillment of the Requirements
for the Degree of Master of Science
at the
University of Tsukuba

Abstract

During the Year-1 running period of Relativistic Heavy Ion Collider (RHIC) at Brookhaven National Laboratory(BNL), Au+Au collisions have been carried out at 130 GeV for the first time in the world.

The Pioneering High Energy Nuclear Interaction eXperiment(PHENIX) is one of the large experiments, which is designed to investigate nuclear collisions with a wide variety of probes, focusing primarily on those produced in the early stages of the collisions.

The global azimuthal event anisotropy is believed to be very sensitive to the early pressure gradient, and therefore it is one of the important variables that help us to understand the early stage of nucleus-nucleus collisions. The event anisotropy can be evaluated with the Fourier expansion of azimuthal distribution of particles, the first two harmonics are called directed and elliptic emission pattern. From Alternating Gradient Synchrotron(AGS) to Super Proton Synchrotron(SPS) experiments, we have learned that the strength of elliptic emission pattern increases gradually with increasing the incident energy. To extract the azimuthal anisotropy, PHENIX has used "Reaction Plane Method" and "Two Particle Azimuthal Correlation Method".

In this thesis, we discuss the elliptic emission pattern of azimuthal anisotropy of particle emission using "Reaction Plane Method" at $\sqrt{s_{NN}}$= 130 GeV Au+Au collisions in RHIC-PHENIX experiment. We have defined the reaction plane with the charged particles measured by the PHENIX Central arm spectrometers that cover mid-rapidity region ($| \eta |< 0.35$). After correcting acceptance with reaction plane flattening, multiplicity and p_t dependence of azimuthal anisotropy are obtained. The results are compared with Two Particle Azimuthal Correlation Method, and other experimental results in RHIC.

We have also measured azimuthal anisotropy of identified particle emission in the limited Time-Of-Flight acceptance, which indicates the possibility of more accurate study after Year-2 experiments at RHIC-PHENIX.

Contents

1 Introduction

1.1 Ultra-Relativistic Heavy Ion Collisions

1.1.1 QGP and Ultra-Relativistic Heavy Ion Collisions

According to the modern theories of the strong interaction based on Quantum ChromoDynamics(QCD), it is expected that the phase transition from hadronic phase to a phase of deconfined quarks and gluons occurs at high energy densities. This new phase of matter is called a Quark Gluon Plasma(QGP).

Fig. 1.1 shows the schematic phase diagram of strongly interacting matter. As the diagram shows, it is expected that a QGP phase transition occurs at a high temperature and/or a high baryon density.
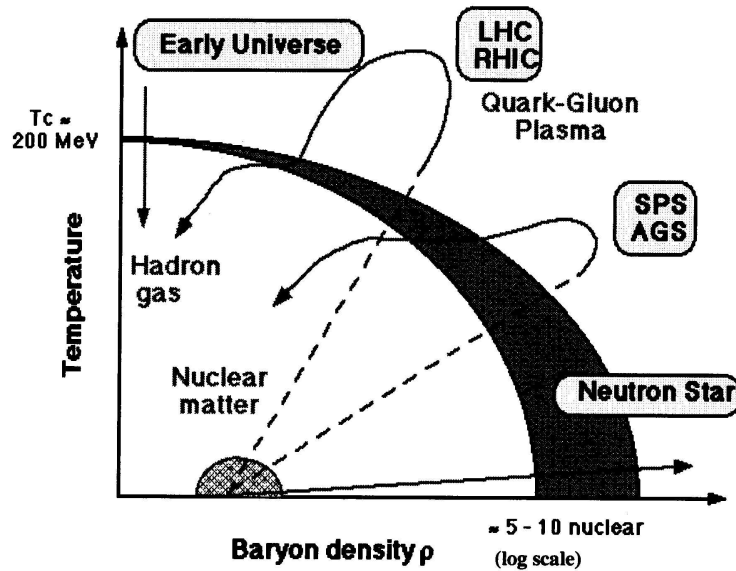

Fig. 1.1: The phase diagram of strongly interacting matter. The hatched region represents where phase transitions are expected to take place. And lines indicate the trajectories in Big Bang evolution, in heavy-ion reactions at AGS,SPS,RHIC and LHC accelerators.

1

To create the condition for a QGP formation, the only way is the heavy ion collisions with ultra-relativistic high energy. The QGP phase might be created when two heavy ions collide head-on with each other at extremely high energy and deposit enough energy in the center of mass. In order to understand the features of the nuclear matter under the extreme conditions and hopefully to capture the QGP signals, many experimental facilities have been constructed and will be constructed in the future. Tab. 1.1 shows the list of current and proposed facilities to accelerations of heavy-ion beams.

Accelerator	Location	Ion beam	Momentum [$A \cdot \mathrm{GeV}/c$]	$\sqrt{s}$ [GeV]	Start
AGS	BNL	^{16}O, ^{28}Si	14.6	5.4	Oct. 1986
		^{197}Au	11.4	4.8	Apr. 1992
SPS	CERN	^{16}O, ^{32}S	200	19.4	Sep. 1986
		^{208}Pb	158	17.4	Nov. 1994
RHIC	BNL	^{197}Au	65	130	Jun. 2000
			100	200	Aug. 2001
LHC	CERN	^{208}Pb	3150	6300	2005 (project)

Tab. 1.1: List of the current and proposed facilities, the ion beams ,the corresponding beam momentum and center of mass energy per nucleon pair.

1.1.2 Participant-Spectator Model

Nuclei are extended objects,and therefore their geometry plays an important role in heavy ion collisions. Fig. 1.2 shows a schematic figure of reaction between Lorentz contracted nuclei in the center of mass frame.

The left figure shows a projectile nucleus and a target nucleus approaching with finite impact parameter b before the collision. The right figure shows state of the two nuclei after the collision. Nucleons which have interacted with other nucleons are called "*participants*". Nucleons which have not interacted going straight with their initial direction are called "*spectators*".

The use of "Participant-Spectator Model" is justified by the fact that at very high energies the size of nucleons is larger than their Compton wavelength and the nuclear radius is larger than the interaction length of ≈ 1.8 fm.
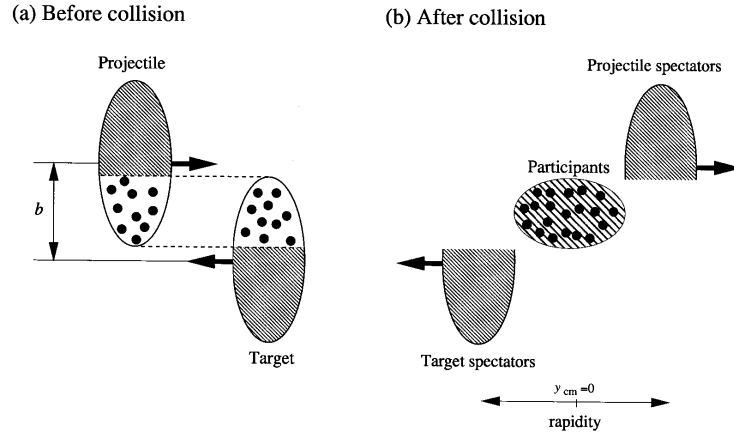
Fig. 1.2: Schematic sketch of participant-spectator model. Left:Before the collision,colliding two Lorentz contracted nuclei in the center of mass frame. Right:After the collision,the nucleons are separated to participants and spectators.

1.2 Kinematics Variables

We define here the kinematic variables commonly used in heavy ion physics.

1.2.1 Transverse Momentum

We take a beam line to be z-axis of a frame. Consider a particle which has momentum $\mathbf{p} = (p_x, p_y, p_z)$ and mass m. The momentum component along the beam direction is called the longitudinal momentum p_z. The components perpendicular to the beam direction are combined and called the transverse momentum which represent the equation (1.1).

$$p_t \equiv \sqrt{p_x^2 + p_y^2} \tag{1.1}$$

The transverse momentum is Lorentz invariant in any frame moving parallel to the z direction. The longitudinal momentum and total energy

$$E \equiv \sqrt{\mathbf{p}^2 + m^2} \tag{1.2}$$

are not Lorentz invariant. And the transverse mass is defined as follows;

$$m_t \equiv \sqrt{p_t^2 + m^2} \tag{1.3}$$

1.2.2 Rapidity

The rapidity is defined as follows;

$$y \equiv \frac{1}{2}\ln\left(\frac{E + p_z}{E - p_z}\right) \tag{1.4}$$

The rapidity has a property in that it is additive under Lorentz transformation,just like a Galilean velocity under Galilean transformation. Therefore, the differential dy is Lorentz invariant. Using equation (1.3) and (1.4), we can easily derive the energy and longitudinal momentum as follows;

$$E = m_t\cosh(y) \tag{1.5}$$
$$p_z = m_t\sinh(y). \tag{1.6}$$

In the relativistic limit$(\mathbf{p} >> m)$, the rapidity becomes as follows;

$$y = \frac{1}{2}\ln\left(\frac{p + p_z}{p - p_z}\right) \tag{1.7}$$
$$= \frac{1}{2}\ln\left(\frac{1 + \cos(\theta)}{1 - \cos(\theta)}\right) \tag{1.8}$$
$$= -\ln\left(\tan(\frac{\theta}{2})\right) \tag{1.9}$$
$$\equiv \eta \tag{1.10}$$

Where θ is the polar angle. The η is called pseudo-rapidity.

2 Azimuthal Anisotropy of Particle Emission

2.1 Overview

The azimuthal anisotropy of particle emission has been studied in nucleus-nucleus collisions with various incident beam energies. It has been found that the azimuthal anisotropy of charged particle emission depends significantly on the incident beam energy.

In this chapter, we present the azimuthal anisotropy of particle emission. We define the reaction plane and three types of emission pattern of azimuthal distributions using mathematical derivation of Fourier expansion. The experimental results up to the SPS energies will be shown.

2.2 Reaction Plane

In each collision of two nuclei, the impact parameter b is defined as a distance between the center of the target and that of the projectile. (Fig. 2.1) The reaction plane is defined the direction of the impact parameter and the beam direction(z-axis). The reaction plane angle Ψ_0 is the azimuthal angle between the reaction plane and horizontal axis of the laboratory as shown in Fig. 2.2.

Experimental determination of reaction plane is one of the key issues in the study of azimuthal anisotropic emission. However, it is not a trivial task in high energy collisions. Since it's not directly measurable, in stead, the anisotropy of emission itself is used to define the reaction plane. In this thesis, we defined the reaction plane by the PHENIX central arm. The detailed method to define the reaction plane in this thesis is described in Sec. 6.1.
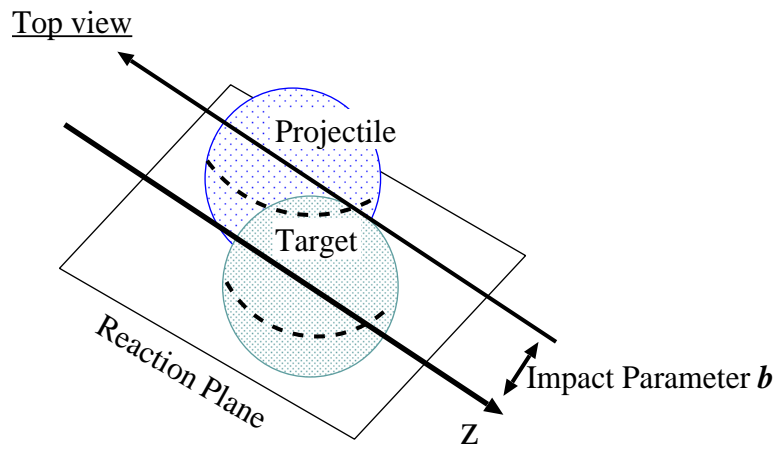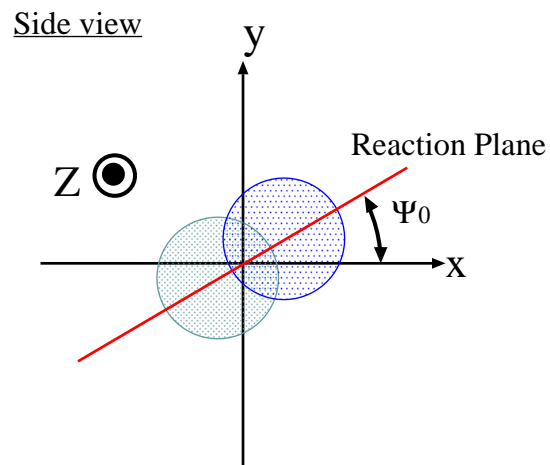
Fig. 2.1: Definition of impact parameter.

Fig. 2.2: Definition of reaction plane.

2.3   Fourier Expansion of Azimuthal Distributions

Procedure of Fourier analysis on an event-by-event basis was developed to analyze Au+Au data of E877 at BNL-AGS [2]. The details of analyzing methods of the azimuthal anisotropy are described in [1]. For simplicity, let us consider the azimuthal distribution of any measurable quantity G such as transverse momentum and charged particle multiplicity. Since $dG/d\phi$ is a periodic function, it can be written in the form of Fourier expansion;

$$\frac{dG}{d\phi} = \frac{G}{2\pi} + \frac{1}{\pi} \sum_{n=1}^{\infty} [a_n \cos(n\phi) + b_n \sin(n\phi)], \tag{2.1}$$

$$a_n = \int_0^{2\pi} \frac{dG}{d\phi} \cos(n\phi) d\phi, \tag{2.2}$$

$$b_n = \int_0^{2\pi} \frac{dG}{d\phi} \sin(n\phi) d\phi. \tag{2.3}$$

The Fourier coefficients of $dG/d\phi$ are given by the integrals with weights proportional to $\cos(n\phi)$ or $\sin(n\phi)$. For the case of a finite number of particles, the integrals becomes simple sums over particles found in the appropriate rapidity;

$$a_n = \sum_{v=1}^{N} G_v \cos(n\phi_v), \tag{2.4}$$

$$b_n = \sum_{v=1}^{N} G_v \sin(n\phi_v), \tag{2.5}$$

where N is the number of the particles generated in a event, G_v and ϕ_v are the value of the observable G and the azimuthal angle of the v-th particle. Each pair of the Fourier coefficients a_n and b_n indicates the presence of the n-th type emission pattern, which can be characterized by the amplitude of

$$v_n = \sqrt{a_n^2 + b_n^2} \tag{2.6}$$

and the azimuthal angle of

$$\Psi_n = \frac{1}{n} \arctan(\frac{a_n}{b_n}) \qquad (0 \le \Psi_n < 2\pi/n). \tag{2.7}$$

We can rewrite the Equation 2.4 and 2.5 by using 2.6 and 2.7;

$$a_n = v_n \cos(n\Psi_n) \tag{2.8}$$

$$b_n = v_n \sin(n\Psi_n) \tag{2.9}$$

From 2.8 and 2.9, we can rewrite Equation 2.1 as the followings;

$$
\begin{aligned}
\frac{dG}{d\phi} &= \frac{G}{2\pi} + \frac{1}{\pi}\sum_{n=1}^{\infty}[a_n\cos(n\phi) + b_n\sin(n\phi)] \\
&= \frac{G}{2\pi} + \frac{1}{\pi}\sum_{n=1}^{\infty}[v_n\cos(n\Psi_n)\cos(n\phi) + v_n\sin(n\Psi_n)\sin(n\phi)] \\
&= \frac{G}{2\pi} + \frac{1}{\pi}\sum_{n=1}^{\infty}[v_n\cos(n(\phi - \Psi_n))] \\
&= \frac{1}{2\pi}(G + 2v_1\cos((\phi - \Psi_1)) + 2v_2\cos(2(\phi - \Psi_2)) + \cdots) \tag{2.10}
\end{aligned}
$$

The azimuthal angle $\Psi_n(n = 1, 2, \ldots)$ corresponds to the reaction plane angle. As will be described later, in this thesis, the reaction plane angle is $\Psi_2(0 \leq \Psi_2 < \pi)$ since reaction plane angle is decided from the elliptic emission pattern of charged particles which enter the PHENIX central arm.

We define three types of particle emission: directed and elliptic emission pattern, which are the two first Fourier component of the azimuthal distribution in non-central collisions; transverse isotropic emission pattern, which is deduced from an analysis of transverse momentum spectra in central collisions.

Fig. 2.3 shows the three types of particle emission pattern. The 0-th order component of Equation 2.10 shows the transverse isotropic emission pattern as shown in Fig. 2.3(a). The 0-th order component is measured by the transverse mass distribution in central nucleus-nucleus collisions.

The first order component as shown in Fig. 2.3(b) is the directed emission pattern which is characterized by the net displacement into particular direction Ψ_1. The coefficient v_1 denotes the magnitude of the directed emission pattern.

The second order component as shown in Fig. 2.3(c) is the elliptic asymmetry with respect to the azimuthal angle of reaction plane($\Psi_1$orΨ_2). This emission pattern is called "elliptic emission pattern" because it shows the simultaneous scaling of the x and y axis and represents an elliptic shape. The coefficient v_2 is proportional to the magnitude of the elliptic emission pattern. For elliptic emission pattern, we call "in-plane elliptic emission " when $v_2 > 0$, and "out-of-plane elliptic emission" when $v_2 < 0$.

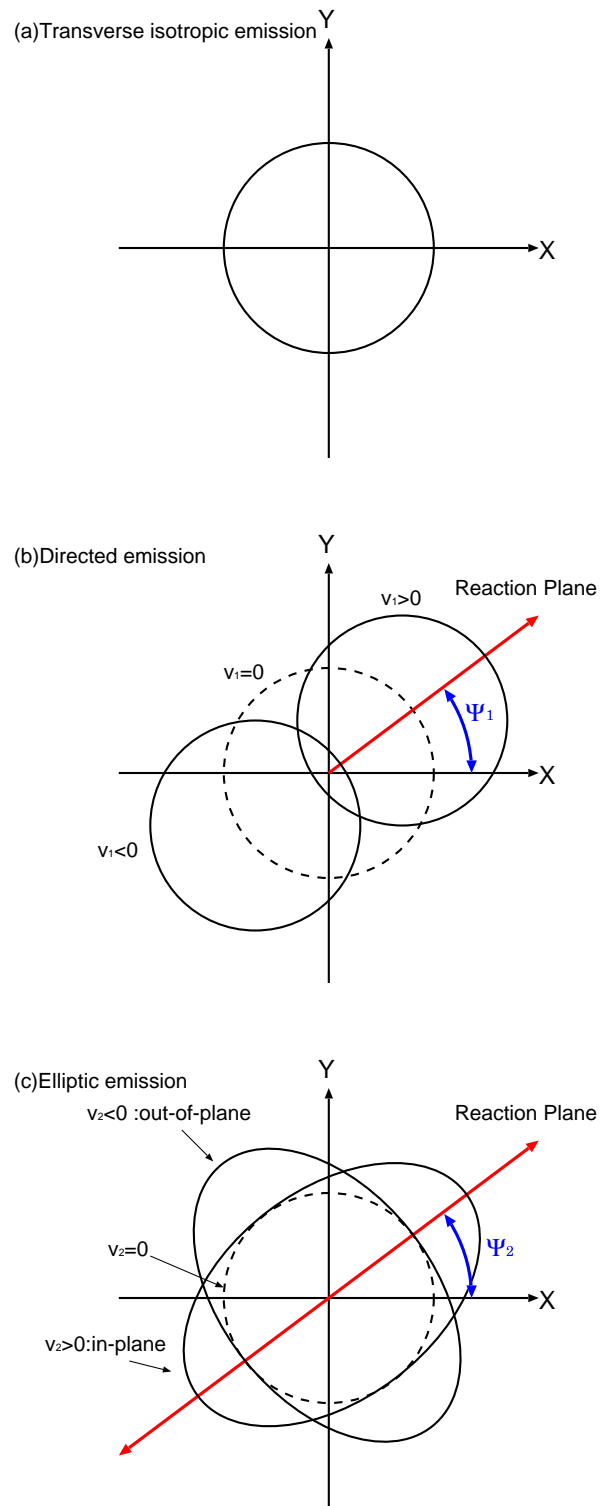Fig. 2.3: Three patterns of particle emission. (a)Transverse isotropic emission pattern (0-th order) (b)Directed emission pattern (First order) (c)Elliptic emission pattern (Second order)

2.4 Directed Emission Pattern(First Order)

The directed emission pattern has been extensively studied from 2 A GeV to 158 A GeV.[3] The magnitude of directed emission depends on the centrality of the collisions, transverse momentum(p_t) and rapidity. [4, 5, 6]

Fig. 2.5 shows the rapidity dependence of $\langle p_x \rangle$ in various beam energy, where $\langle p_x \rangle$ is the average value of the transverse momentum projected on the reaction plane. When beam energy is exceeded 10 A GeV, the slope of $\langle p_x \rangle$ has become zero and flat v_1 at the mid-rapidity. In the special case, when it has negative slope in the mid-rapidity, it is called "Third flow component". According to the fluid dynamical calculation (Fig. 2.4,[7]), This signal is expected as QGP creation signal.
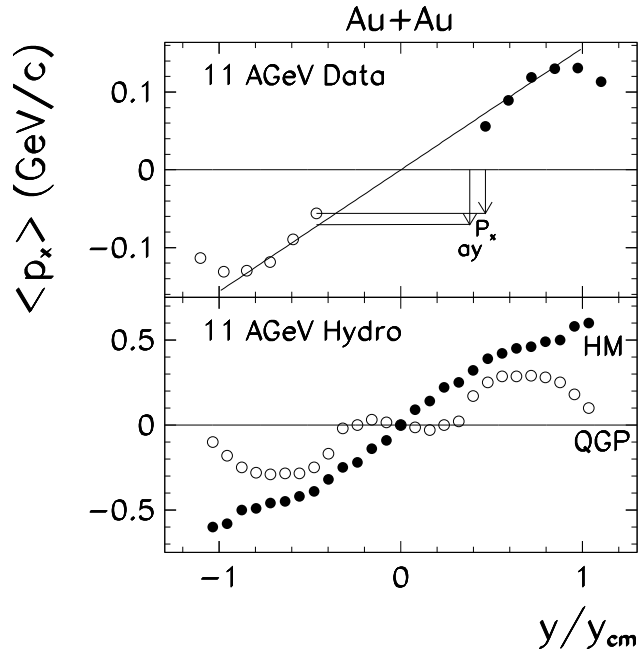

Fig. 2.4: Upper:Experimental data. Lower:A typical example for fluid dynamical calculations with Hadronic and QGP equation of state [7].
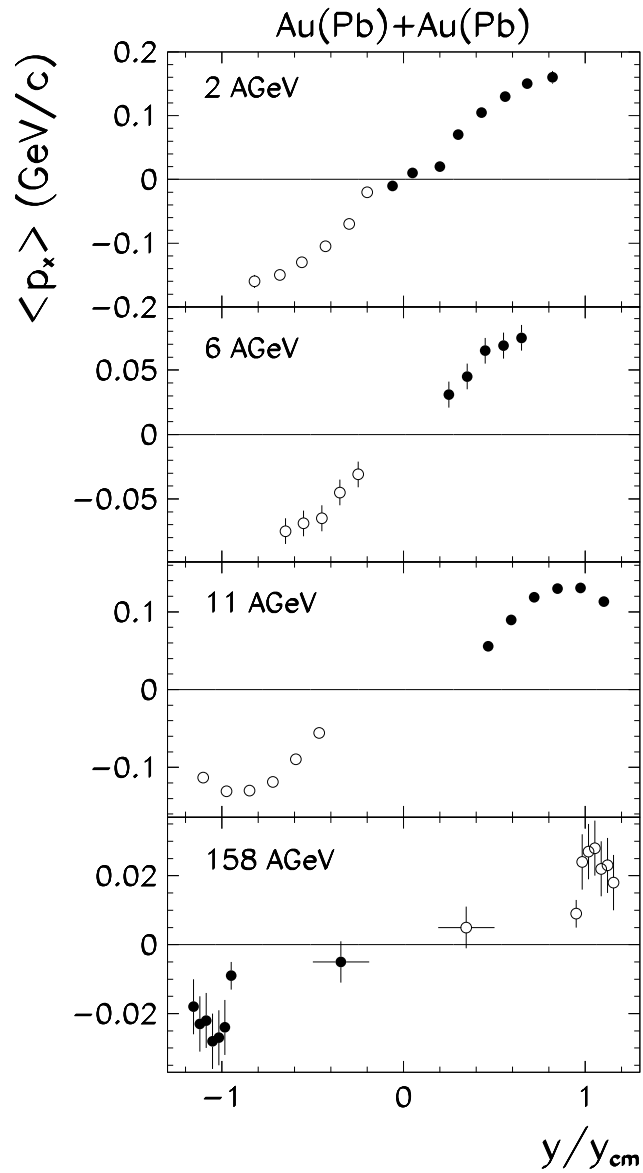
Fig. 2.5: Rapidity dependence of $\langle p_x \rangle$ projected on the reaction plane in various incident energy. $\langle p_x \rangle$ becomes zero more than 10 A GeV at mid-rapidity region [7].

2.5   Elliptic Emission Pattern(Second Order)

While directed emission pattern keeps the same sign from SIS to SPS energies, elliptic emission pattern has a transition from out-of-plane to in-plane at higher energy regions. Fig. 2.6 shows the strength of elliptic emission pattern as a function of incident beam energy per nucleon in the laboratory flame.

At BEVALAC and SIS energies around 1 A GeV, the participant nucleons, which are compressed in the region where the target and projectile overlap, can not escape in the reaction plane due to the presence of the spectator nucleons, it produces out-of-plane elliptic emission. This is called "squeeze-out". This out-of-plane elliptic emission pattern is interpreted due to the shadowing effect. The out-of-plane elliptic emission pattern is maximum at about 400 A MeV of beam energy.

The transition from out-of-plane to in-plane emission pattern has occurred the result of the Lorentz contraction at relativistic energies. Spectators leave the participants region after a time of $2R/\gamma$. Later, outgoing particles are free to escape anywhere in the transverse space. Since the overlap region has a smaller size along the impact parameter, the pressure gradient is larger in the reaction plane. This produces in-plane elliptic emission pattern.

However, the interesting result is found in the WA98 experiment that elliptic emission of K+ has a "out-of-plane" emission pattern while pion has a "in-plane" emission pattern [8, 9]. This result may indicate that it is not enough to understand the Kaon's elliptic emission pattern using only hydro-dynamical explanations.

In the year-2000, the Relativistic Heavy Ion Collider(RHIC,see Chap. 3) has started to take the Au+Au collisions data. Many interesting results are obtained from STAR [10, 11], PHOBOS [12], and PHENIX [13] experiment. (The PHENIX has adopted "Two Particle Correlation Method". Difference of analysis methods are discussed next section.)
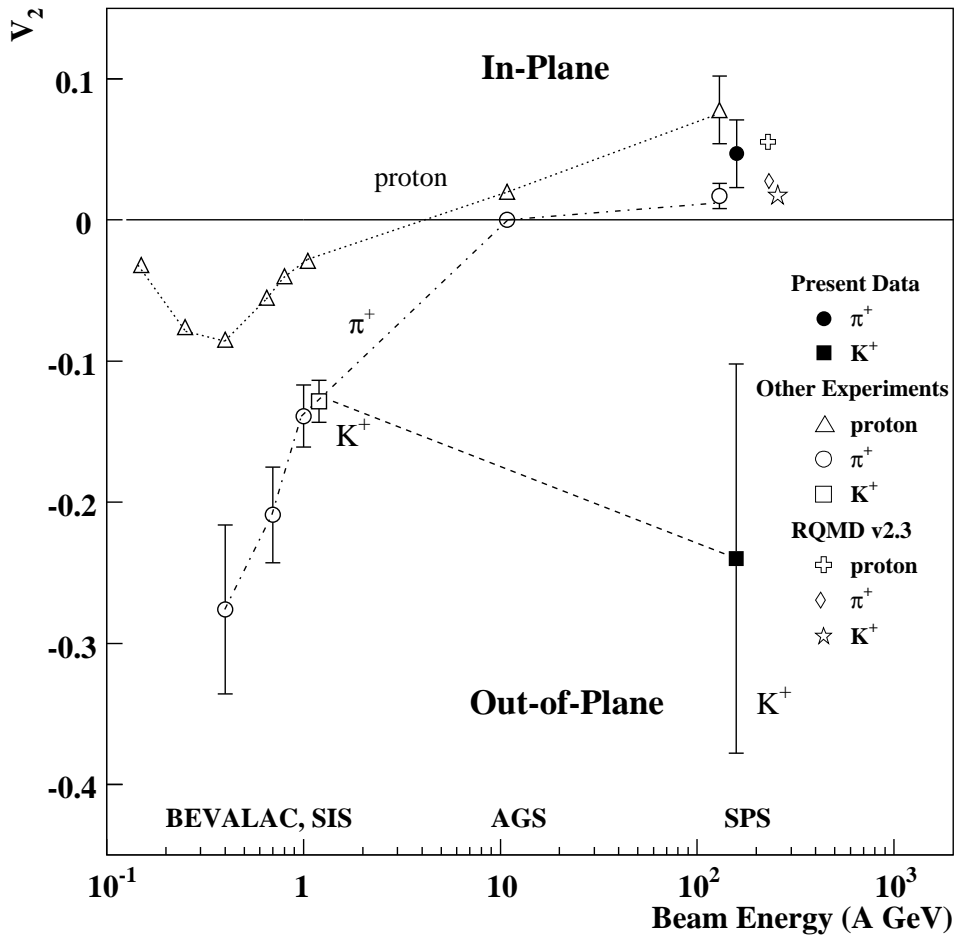
Fig. 2.6: Incident energy dependence of elliptic emission pattern strength v_2 [8, 9].

14

2.6 Analysis methods for Azimuthal Anisotropy of particle emission

There are several methods for the analysis of azimuthally anisotropic emission [1].

The analysis methods are roughly divided into two groups, which are "Two Particle Azimuthal Correlation Method" and "Reaction Plane Method". Fig. 2.7 shows schematic description of both methods.

First one has already been adopted in the PHENIX experiment [13]. However, the other one is not adopted yet. Because there are no experiences of analysis using "Reaction Plane Method" in limited acceptance detector such as the PHENIX. To compare with the various methods is important, which will be not only systematic uncertainty check, but study of other sources of generating azimuthal anisotropy such as Jets,HBT,Resonance Decay and Momentum conservation.
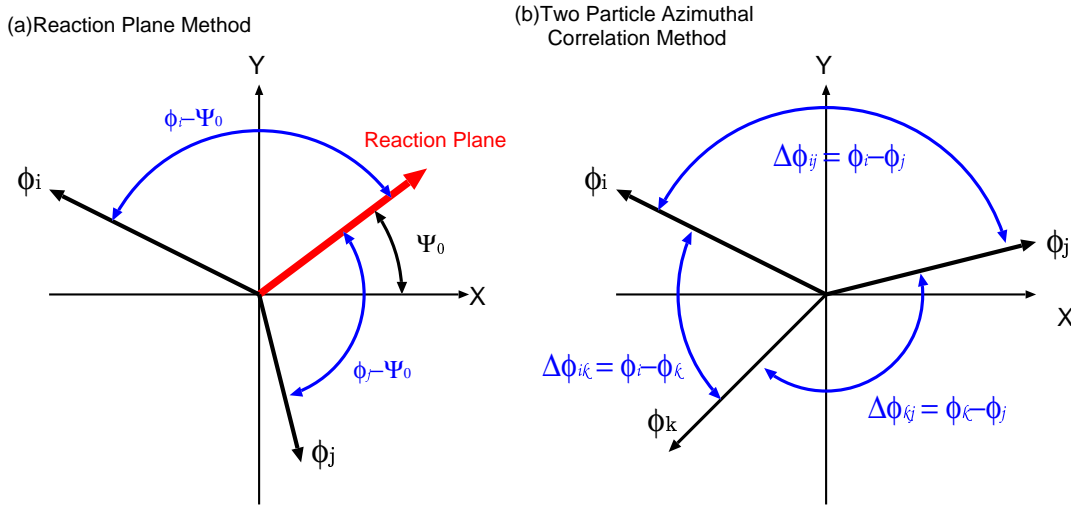
Fig. 2.7: The schematic description of two different kinds of methods for azimuthal anisotropy analysis. (a)Reaction Plane Method. (b)Two Particle Azimuthal Correlation Method.

The features and differences of both methods are described next section.

2.6.1 Two Particle Azimuthal Correlation Method

"Two Particle Azimuthal Correlation Method" can be written following formula;

$$\frac{dN^{pairs}}{d(\Delta\phi)} \propto (1 + \sum_{n=1}^{\infty} 2v_n^{obs} \cos(n\Delta\phi)) \tag{2.11}$$

$$v_n = \sqrt{v_n^{obs}} \qquad (2.12)$$

where $\Delta\phi$ is angle difference between pairs of emitted particles ($\Delta\phi = \phi_1 - \phi_2$). The magnitude of the azimuthal anisotropy is characterized by the square of the Fourier coefficient(Equation 2.12). The main features of this method are as follows;

- Reaction plane determination is not required.

- There are many particle combinations, which can reduce statistical error.

- Acceptance correction can be done by event mixing method.

- May sensitive to Jet especially at high p_t region.

- "Signal" is small. It does not imply that the "Signal to noise ratio" is small.

2.6.2 Reaction Plane Method

"Reaction Plane Method" can be written by Fourier expansion as followings;

$$\frac{dN}{d(\phi - \Psi_0)} = N_0 \left(1 + \sum_{n=1}^{\infty} 2 v_n^{obs} \cos(n(\phi - \Psi_0)) \right) \qquad (2.13)$$

$$v_n = \frac{v_n^{obs}}{Resolution} \qquad (2.14)$$

where ϕ is the azimuthal angle of emitted particles, Ψ_0 is the reaction plane angle. Strength of azimuthal anisotropy v_n can be obtained by dividing the observed coefficients v_n^{obs} by the reaction plane resolution, which is estimated from the correlation of the planes of independent sub-events(See Chapter. 6 in details).

The main features of this method are as follows;

- Reaction plane determination is required.

- Study of azimuthal anisotropy of identified particles can be done with respect to the reaction plane.

- Sensitivity to other sources of azimuthal correlations might be different from "Two Particle Azimuthal Correlation Method".

- If the detector does not have full azimuthal acceptance, which can be corrected by "shifting method" to flatten the reaction plane distribution.

- Correction factor for the "Ghost Track" might be smaller than "Two Particle Azimuthal Correlation Method".

- If the detector has "Small" acceptance, systematic error will be increase because reaction plane resolution become worse especially central collision region.

2.7 Simulation Study of Two different kinds of Methods

In this section, we present the simulation results [1] to study the difference of two methods using the limited acceptance detector such as PHENIX experiment [18].

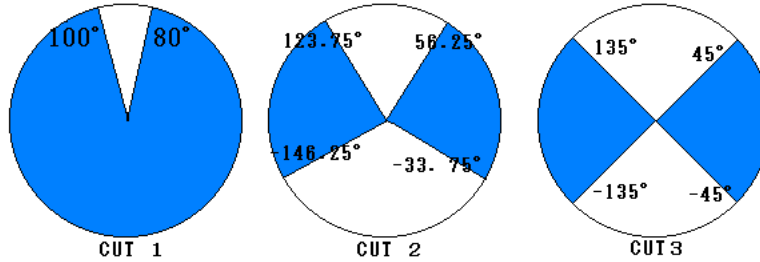In this simulation, 3-types of detector acceptances are applied as shown Fig. 2.8.

Fig. 2.8: Acceptance distribution used in simulation. Set-up2 is same as the PHENIX acceptance.

The azimuthal anisotropy of elliptic emission pattern(v_2) is generated with respect to randomly rotated reaction plane. (Details of calculation method is shown Chapter. 6)

2.7.1 Simulation Using "Reaction Plane Method"

When we calculate the reaction plane, we get the reaction plane distribution shown as the solid line histogram in the Fig. 2.9, because of the acceptance of the PHENIX central arm. This reaction plane is flattened as the dashed histogram in Fig. 2.9, with the standard technique "shifting method". The reconstructed v_2 can be extracted from the solid line histogram in Fig. 2.10, where the amplitude of the cos function is smaller about factor of 3 compared to the originally generated dashed, this is because the reaction plane used to reconstruct v_2 has finite resolution. Table. 2.1 shows the result of simulation using "Reaction Plane Method".

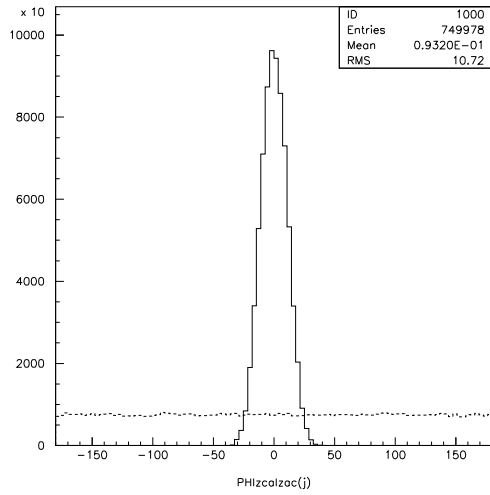[1]S.Esumi and M.Shindo(University of Tsukuba) had carried out this simulation.

18

Fig. 2.9: Reaction plane distribution in Set-up2. Solid line histogram is raw distribution. Dashed line histogram is distribution after flattening correction.
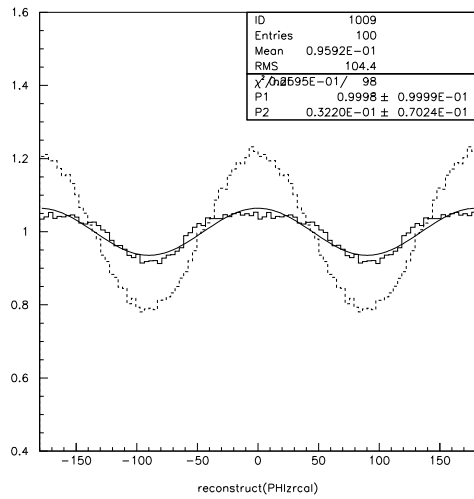

Fig. 2.10: $\phi - \Psi_0$ distribution in Set-up2. Dashed line histogram is distribution before flattening correction, and solid line histogram is after flattening correction.

	v_2^{gen}	$v_2^{fitting}$	v_2^{cal}
Set-up1	0.05	5.08×10^{-2}	5.08×10^{-2}
Set-up1	0.1	9.99×10^{-2}	9.99×10^{-2}
Set-up2	0.05	6.76×10^{-2}	6.72×10^{-2}
Set-up2	0.1	0.10×10^{-2}	0.10×10^{-2}
Set-up3	0.05	4.27×10^{-2}	4.27×10^{-3}
Set-up3	0.1	9.92×10^{-2}	9.83×10^{-2}

Tab. 2.1: Simulation results with "Reaction Plane Method"

2.7.2 Simulation Using "Two Particle Azimuthal Correlation Method"

Using this analysis method, we do not need to define a reaction plane, instead the mixed event is used to normalize the $\Delta\phi$ distribution of two charged particle measured in the central arm in order to remove the detector acceptance effect. In this simulation, the original anisotropy of azimuthal distribution can be reconstructed by square root of the measured v_2 in the mixed event normalized two particle azimuthal distribution as Fig. 2.11. The results is shown Fig. 2.12, which indicates that this methods can reconstruct original v_2 if there is no other sources of azimuthal correlations.
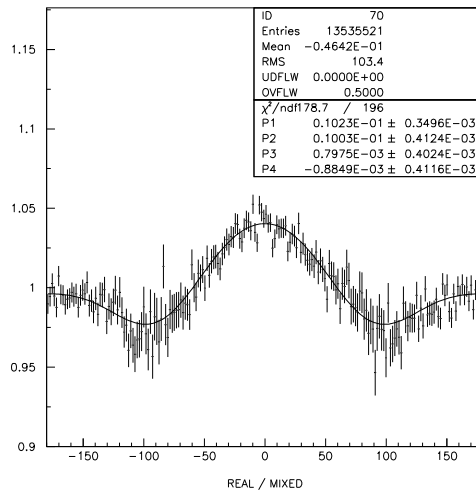
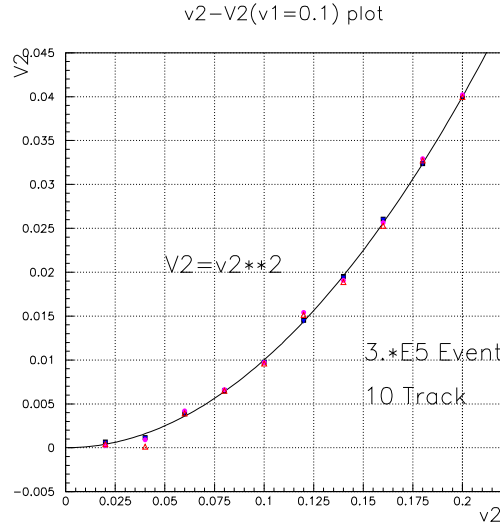Fig. 2.11: $\Delta\phi$ distribution in Set-up2.

Fig. 2.12: The results of using Two Particle Correlation Method. X-axis is generated v_2, Y-axis is reconstructed v_2^{obs}. Clear correlation of $v_2 = \sqrt{v_2^{obs}}$ is shown.

2.7.3 Results of Simulation

Both two methods have been made sure that they properly reconstruct the originally generated v_2 with the PHENIX central arm acceptance, if there is no other sources of azimuthal correlations. However if there is other other sources of generating azimuthal anisotropy, the sensitivity might be different between those two methods, so the quantitative comparison between results of those two methods on the experimental data is interesting.

2.8 Thesis Motivation

This thesis is motivated by the following points,

- Estimate the possibility of the "Reaction Plane Method" using the PHENIX experimental data.

- Analyzing azimuthal anisotropy of particle emission in $\sqrt{s}_{NN} = 130$ GeV Au+Au Collisions at RHIC-PHENIX.

3　The PHENIX Experiment

3.1　Overview of the RHIC

Relativistic Heavy Ion Collider(RHIC), which can create the highest energy density in the world at present, is in Brookhaven National Laboratory(BNL) in New York. Fig. 3.1 shows collider complex of RHIC.

RHIC has two circular rings of super conducting magnets lying side by side in an underground tunnel that is 3.8 kilo meters in circumference.

Gold ions for RHIC collisions originate in the Tandem Van de Graaff accelerator and proceed to the Booster and the AGS, getting accelerated to ever higher energy at each stage. Bunches of about one billion ions for each ring are extracted from the AGS and transferred to each of the two collider rings. After each ring filled, the ion beams are accelerated to a top energy ranging. (Maximum energy is 100 GeV for Au, 250 GeV for Proton)

Detectors named BRAHMS(Broad Range Hadron Magnetic Spectrometers , located 2 o'clock), PHOBOS(named for a moon of Mars, located 10 o'clock) , STAR(the Solenoidal Tracker At RHIC, located 6 o'clock), and PHENIX(located 8 o'clock) are sited at the interaction points where the two beams cross to examine the data from collisions. Two more intersection points are potentially available for future experiments.
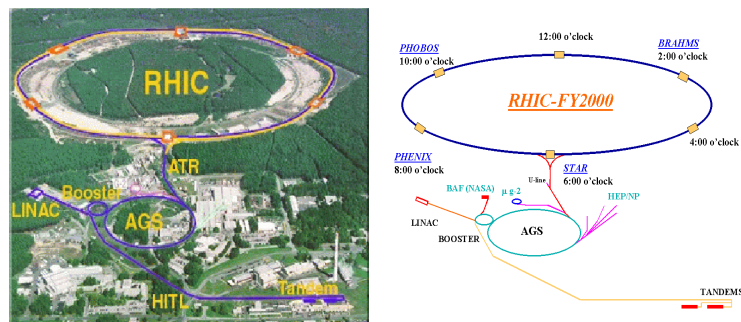

Fig. 3.1: Left:The RHIC accelerator complex. Right:The schematic diagram of RHIC complex in Year-1 operation.

3.2 Overview of the PHENIX Experiment

The primary goals of the PHENIX experiment are the detection of QGP signals and characterization of its physics properties. In order to achieve these goals, the PHENIX detector utilizes a variety of detector technologies. The PHENIX detector has a large capability to characterize the collisions, a pair of central spectrometers at mid-rapidity to measure electrons,hadrons,and photons and a pair of forward spectrometers to measure muons. The acceptance of the PHENIX is shown in Fig. 3.2.
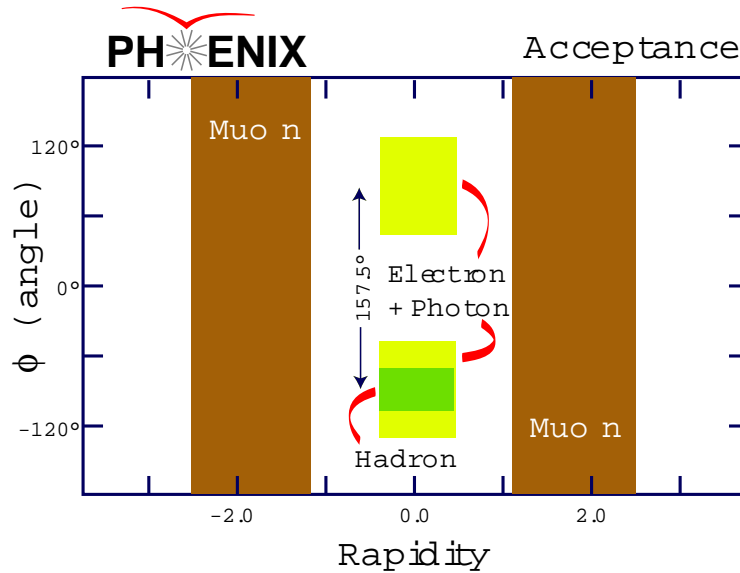
Fig. 3.2: The PHENIX acceptance of hadrons and leptons.

The PHENIX detector consists of a number of subsystems. Fig. 3.3 shows overview of the PHENIX detector. Main features of each subsystems are shown in Tab. 3.1.
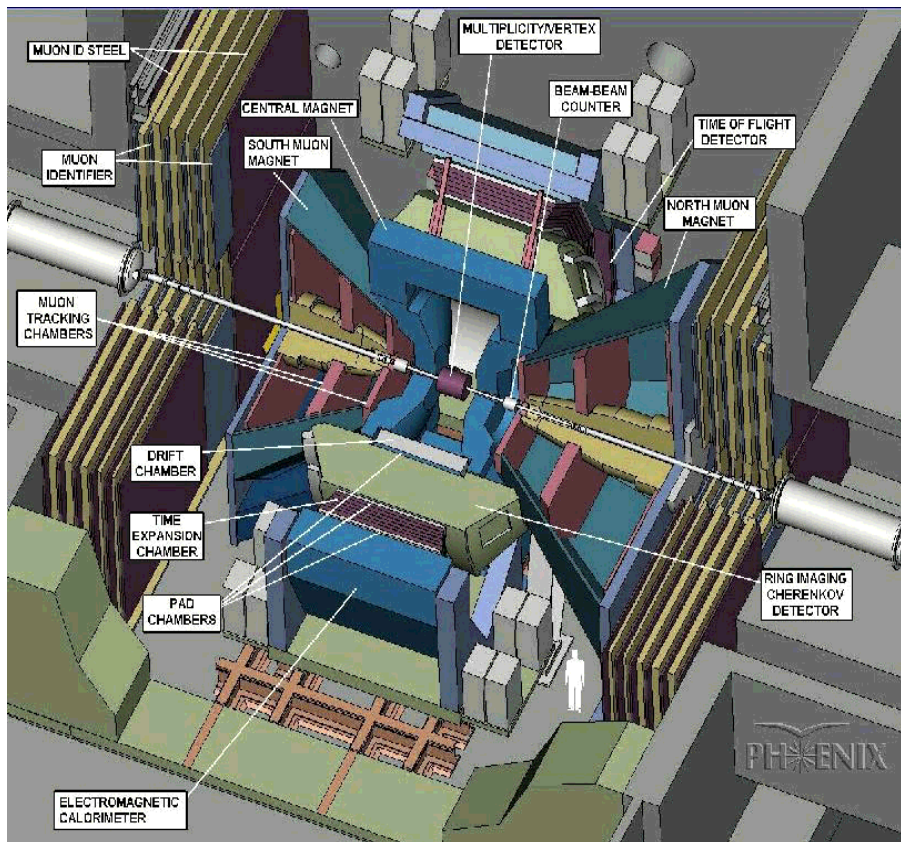
Fig. 3.3: Overview of the PHENIX detector. Labeled arrows point to the major detector subsystems.

24

Tab. 3.1: The PHENIX Detector Summary.

Element	$\Delta\eta$	$\Delta\phi$	Purpose and Special Features
Magnet: central (CM)	± 0.35	$360°$	Up to 1.15 T·m.
muon (MMS)	-1.1 to -2.2	$360°$	0.72 T·m for $\eta = 2$
muon (MMN)	1.1 to 2.4	$360°$	0.72 T·m for $\eta = 2$
Silicon (MVD)	± 2.6	$360°$	$d^2N/d\eta d\phi$, precise vertex, reaction plane determination
Beam-beam (BBC)	$\pm(3.1$ to $3.9)$	$360°$	Start timing, fast vertex.
NTC	$\pm(1$ to $2)$	$320°$	Extend coverage of BBC.
ZDC	± 2 mrad	$360°$	Minimum bias trigger.
Drift chambers (DC)	± 0.35	$90°\times 2$	Good momentum and mass resolution, $\Delta m/m = 0.4\%$ at $m = 1$GeV.
Pad chambers (PC)	± 0.35	$90°\times 2$	Pattern recognition, tracking for non bend direction.
TEC	± 0.35	$90°$	Pattern recognition, dE/dx.
RICH	± 0.35	$90°\times 2$	Electron identification.
ToF	± 0.35	$45°$	Good hadron identification, $\sigma <100$ ps.
T0	± 0.35	$45°$	Improve ToF timing.
PbSc	± 0.38	$90°\times 1.5$	Photon and electron detection.
PbGl	± 0.35	$45°$	Good e/π separation at $p > 1$ GeV/c by EM shower and $p < 0.35$ GeV/c by ToF. K/π separation at 1 GeV/c by ToF for dE/dx for PbSc.
μ tracker: (μTS)	-1.15 to -2.25	$360°$	Tracking for muons.
(μTN)	1.15 to 2.44	$360°$	Muon tracker north installed for year-3
μ identifier: (μIDS)	-1.15 to -2.25	$360°$	Steel absorbers and Iarocci tubes for muon/hadron separation.
(μIDN)	1.15 to 2.44	$360°$	Muon identifier north installed for year-3

3.2.1 Central Magnet

The PHENIX magnet system is composed of three spectrometer magnets. The Central Magnet (CM) is energized by two pairs of concentric coils and provides an approximately axially symmetric field. This allows momentum analysis of charged particles in the polar angle range from 70° to 110°. The north and south Muon Magnets (MMN and MMS) use solenoid coils to produce a radial magnetic field for muon analysis. They each cover a pseudo-rapidity interval of 1.1 to 2.3 and full azimuth. Each of the three magnets provides a field integral of about 0.8 Tesla-meters.
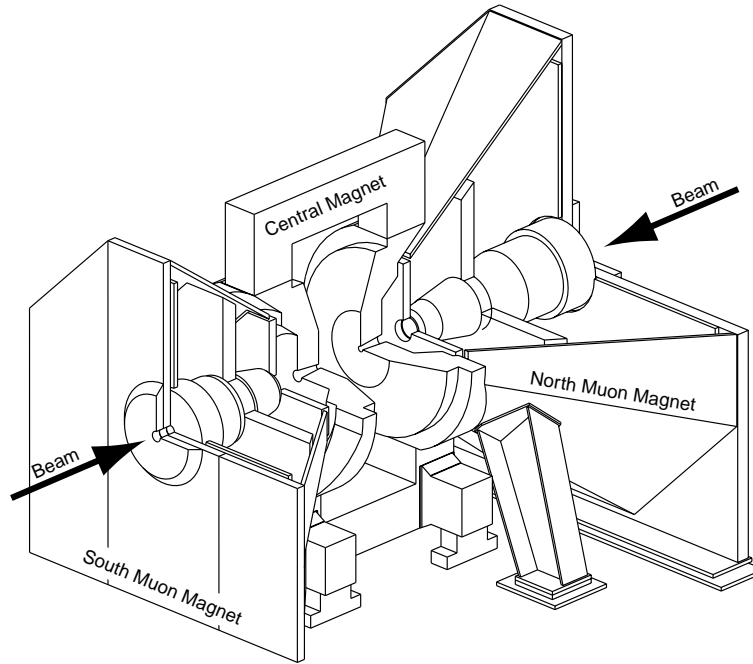
Fig. 3.4: Line drawings of the PHENIX magnets. Arrows indicate the beam line of the colliding beams in RHIC.

3.2.2 Inner Detectors

Beam-Beam Counters(BBC)

The main purpose of BBC is to provide the start time for the Time-Of-Flight measurement,to produce a signal for the PHENIX Level-1 trigger and to decide the collision vertex point along the beam axis. The BBC consists of two identical sets of counters installed on both sides of the beam axis and the BBC are located 144cm

from the center of the collision point. This corresponds to a pseudo-rapidity range from 3.0 to 3.9 over the full azimuth. Start timing resolution of the BBC have achieved about 40 ps.

Zero Degree Calorimeters(ZDC)

The ZDC measure the energy deposit by spectator neutrons during the collisions and make a signal for the PHENIX Level-1 trigger. Each ZDC is located 18 meters up and downstream from the interaction point along the beam axis.

Multiplicity Vertex Detector(MVD)

The MVD is made up of two concentric barrels of silicon strip detectors and two disk-shaped endcaps of silicon pad detectors located $\pm 35cm$ from the center of collision point. The MVD measure the multiplicity of charged particles produced in each event.

3.2.3   Central Arm Spectrometers

Drift Chambers(DCH)

The role of DCH is measuring charged particle trajectories in the r-ϕ direction to determine p_t.

The DCH are installed each(west and east)central arm. Each detector is located in the region from 2.02 to 2.46 meters from the z-axis and 1.8 meters long the beam direction. This places them in a residual magnetic field.(0.6kG maximum) Fig. 3.5 shows construction of the DCH.
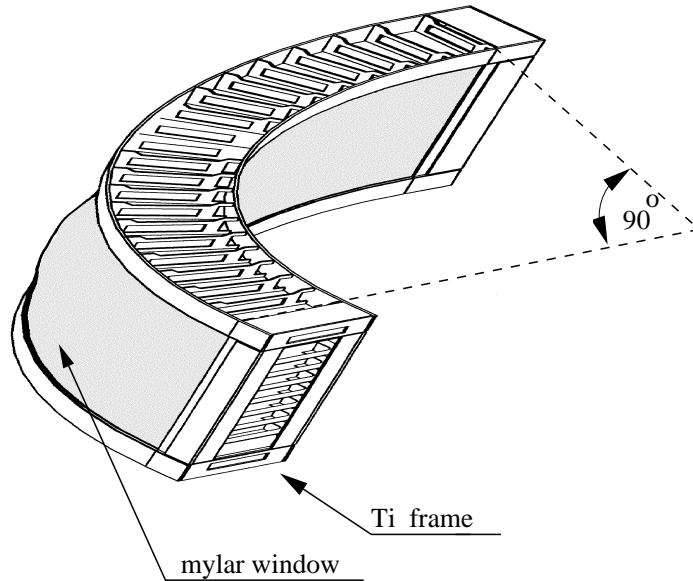

Fig. 3.5: The DCH construction

The DCH volume is decided by a cylindrical titanium frame defining the azimuthal and beam-axis limits and each frame is divided in 20 equal sectors covering 4.5° in ϕ direction. There are six types wires; X1,U1,V1,X2,U2,V2. The X1 and X2 wire run in parallel to the beam axis to decide precise track position in r-ϕ direction. The U,V type wires are called stereo wires and are titled with respect to the z-axis. The stereo wires provide the z information.

Pad Chambers(PC)

The PC are multi-wire proportional chambers that form three separate layers of the PHENIX central tracking system. Each layer is called PC1,PC2,PC3. The de-
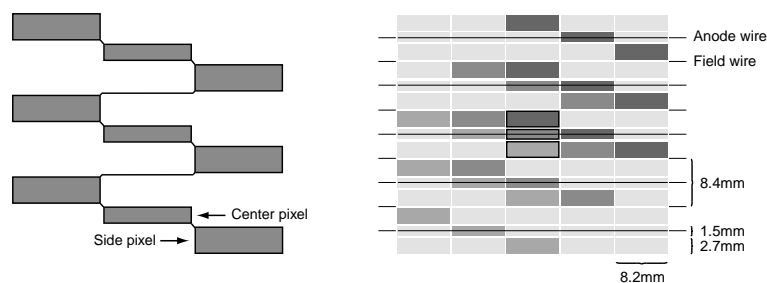
Fig. 3.6: The pad and pixel geometry(left). A cell defined by three pixels is at the center of the right picture.

tector consist of a single plane of wires and cathode pad to read out. One cathode pad is separated into an array of pixels. Nine pixels are connected together electronically to form a pad, the basic element of the detector. Fig. 3.6 shows the pad and pixel geometry. The PC measure 3-D space position along the straight line particle trajectories outside the magnetic field. Especially, the information provided by PC1 is used to determine the three-dimensional momentum vector at the exit of the DCH.

Time Expansion Chambers(TEC)

The TEC performs a number of functions in the PHENIX. It measures all charged particles passing through its active area, providing direction vectors that are matched to additional track information from the DCH and PC. The track information is used to solve the complex pattern recognition problems in the high multiplicity situation. In addition the TEC measure the charged particle ionization energy losses (dE/dx) from which it can be possible particle identification, especially electron and pion.

Time Of Flight Detector(TOF)

The TOF detector is a primary particle identification device for charged hadrons in PHENIX. The TOF is located 5.1 meters away from the center of vertex point. The detector consist of 10 panels of TOF walls. One wall consist of 96 scintillators and 196 photo-multiplier tubes(PMTs) which are read out at both ends of scintillator. The slat is oriented along the r-ϕ direction and provides time and longitudinal position information of particles that hit the slat. Fig. 3.7 shows the schematic view of one panel of TOF.

A total 10 panels are installed and operated at the Year-1 in PHENIX (Fig. 3.8).

The designed time resolution of TOF is 80 ps, which corresponds to the π/K separation up to 2.4 GeV/c and $K/Proton$ separation up to 4.0 GeV/c in 4 σ.
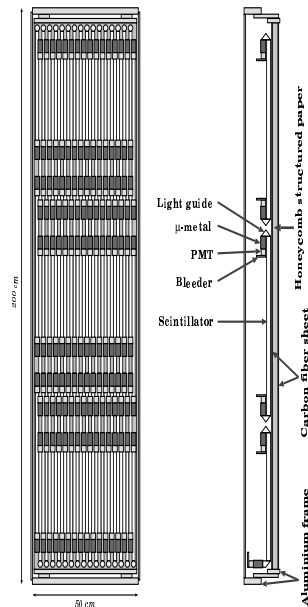

Fig. 3.7: Schematic diagram of one panel of TOF. One panel includes 96 plastic scintillation counters with PMTs at both ends.

Ring Image CHerenkov counters(RICH)

The RICH detectors are installed each of the PHENIX central arm. The RICH the primary devices for separation of electrons from the large numbers of π. In combination with the EMCal in each arm and the TEC in one arm, the goal is to limit the false identification of hadrons as e^+ and e^- to less than 1 per 10^4, for momenta below the Cherenkov threshold.

ElectroMagnetic Calorimeters(EMCal)

The PHENIX Electromagnetic Calorimeter (EMCal) is used to measure the spatial position and energy of electrons and photons. It covers the full central spectrometer acceptance of $70° \leq \theta \leq 110°$ with two walls subtending $90°$ in azimuth. One wall comprises four sectors of a Lead-Scintillator (PbSc) sampling calorimeter and the other has two sectors of PbSc and two of a Lead-Glass (PbGl) Cherenkov calorimeter. Both detectors have very good energy, spatial and timing resolution,
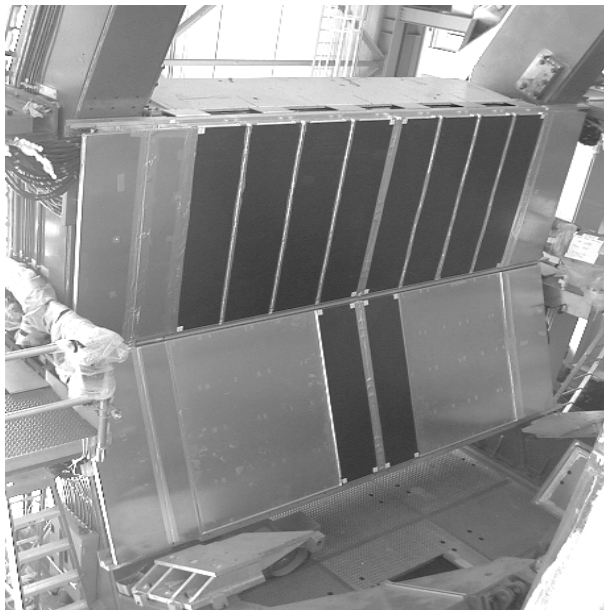
Fig. 3.8: A photograph of TOF detector which is mounted on the PHENIX East Arm.

while the PbSc excels in timing and the PbGl in energy measurements.

3.2.4 Muon Spectrometers

The primary role of the muon spectrometers is identify and track muons. The spectrometers give the PHENIX acceptance for muons decaying into lepton pairs emitted at rapidities of y=-1.15 to -2.25 for the south arm and y=1.15 to 2.44 for the north arm. These two forward spectrometers contain a muon tracker followed by a muon identifier and have full azimuthal acceptance. The muon trackers consist of three stations of multi-plane drift chambers that provide precision tracking. And the muon identifiers consist of alternating layers of steel absorber and low resolution tracking layers of streamer tubes of the Iarocci type. With this combination the π contamination of identified muons is typically 3×10^{-3}. The north muon spectrometers will be installed before the Year-3 run.

4 Run Condition

4.1 Beam Energy and Target

In Year-1(2000) of running at the RHIC, each Au beam were accelated up to 65 GeV($\gamma \approx 70$) which correspond to $\sqrt{s_{NN}} = 130GeV$. Fig. 4.1 shows the Year-1 configuration of the PHENIX detector.

The design value is 100 GeV for each ring($\gamma \approx 107$), which correspond to $\sqrt{s_{NN}} = 200GeV$. From Year-2(2001), RHIC has been operated in full energy.

4.2 Trigger

The event trigger is made by ZDC OR BBC. Total number of minimum bias event is about 1.6 M.
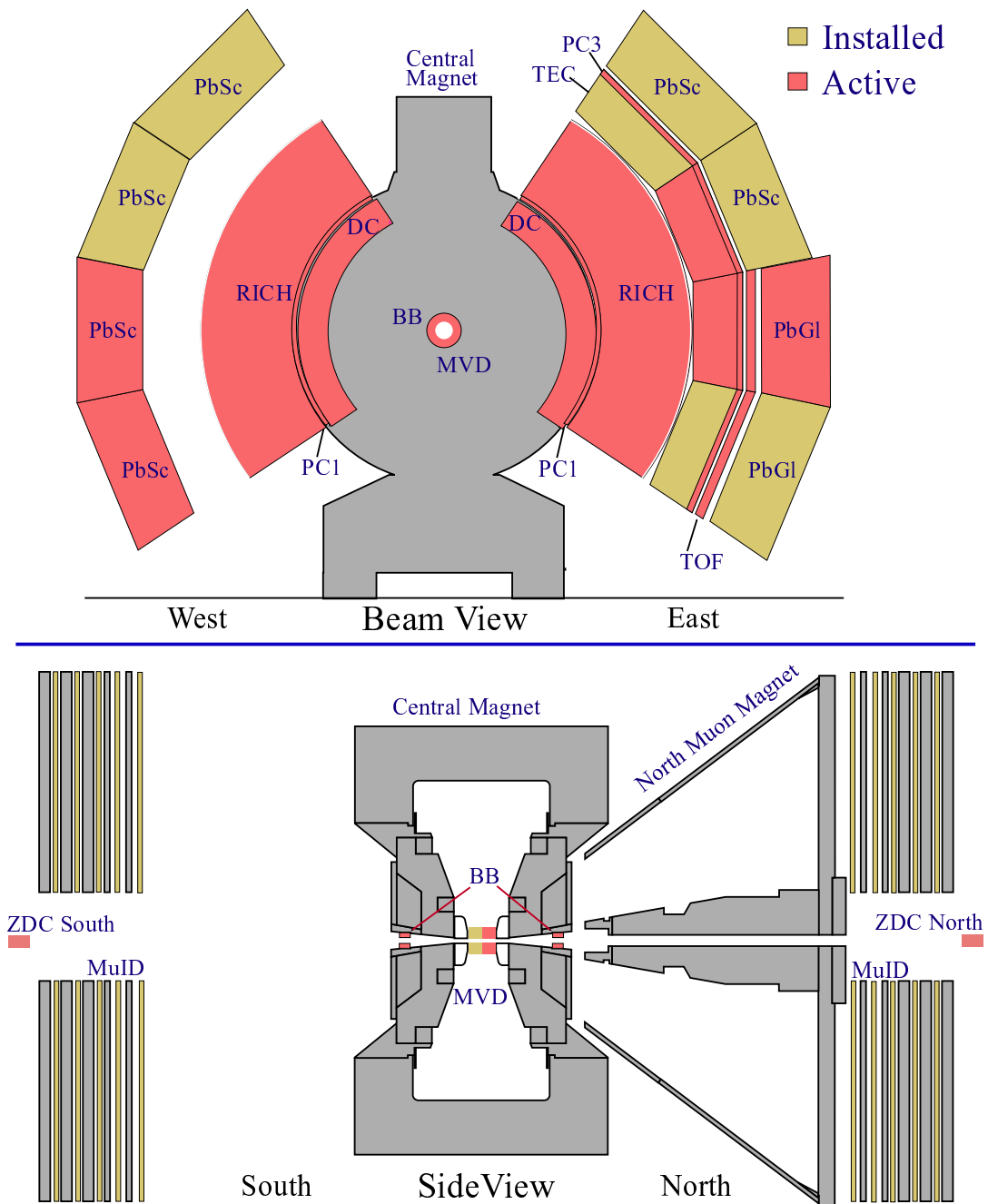
32

Fig. 4.1: Year-1 configuration of the PHENIX detector.

5 Data Reduction

5.1 Track Reconstruction

We have selected only the tracks that have all three coordinates information. This can be determined by selecting those tracks with "Track Quality" bit> 20. The track reconstruction precedures are following;

- Associates hits in either X1 or X2, or both wires to each track. The x and y position of the track in PHENIX global coordinates at the drift chamber reference radius can be determined by this associates.

- Searches all the possible hit positions of charged particle in ϕ direction in the PC1 for each track.

- Projects the vertex decided by BBC and the PC1 hit positions into the xy-plane.

- Fits a straight line to the DCH points in X1 and X2 , the BBC vertex , and the PC1 closest point.

- Intersects this line with a cylinder positioned at the drift chamber reference radius.

- In high multiplicity events, there are some difficulty for choosing the closest point at PC1. Then the algorithm uses the UV wire information.

As a result, this algorithm make variety possible tracks. Therefore, each reconstructed track has assigned to it a quality bit which indicates whether or not the track has all three coordinates information. The "Track Quality" bits are shown in Tab. 5.1 and Fig. 5.1 shows the track quality distributions.

Track Quality	X1 2^0	X2 2^1	PC1 2^2	UV 2^3	Vertex 2^4
1	1	0	0	0	0
2	0	1	0	0	0
3	1	1	0	0	0
21	1	0	1	0	1
22	0	1	1	0	1
23	1	1	1	0	1
29	1	0	1	1	1
30	0	1	1	1	1
31	1	1	1	1	1

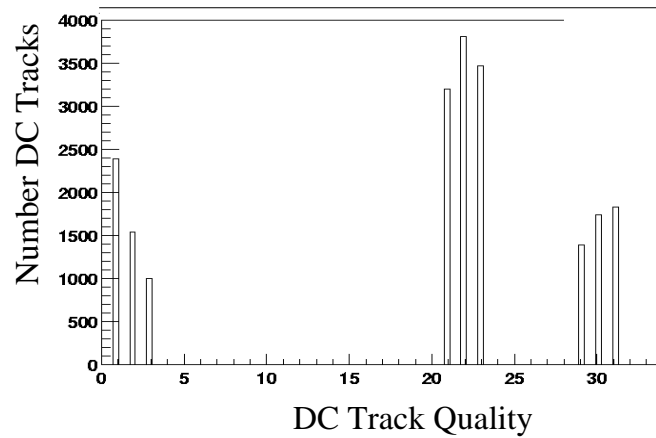Tab. 5.1: Track quality definition

Fig. 5.1: Track quality distribution.

5.2   Particle Identification

Here, the schematic idea of particle identification is presented. Detail descriptions are found in [14, 15].

Flight time of each particle is determined following equation;

$$T_{flight} = t_{TOF} - t_0^{BBC} \tag{5.1}$$

where, t_{TOF} is the time read for the TOF, t_0^{BBC} is the start timing from the BBC.

And β can be represented equation 5.2;

$$\beta = \frac{L}{c \cdot T_{flight}} \tag{5.2}$$

where L is a flight pass which is defined the distance between TOF and vertex.

We can calculate mass distribution as follows using $p = m\beta\gamma$ ($\gamma = \sqrt{1 - \beta^2}$) relation and equation 5.2,

$$m^2 = p^2\left(\left(\frac{T_{flight} \cdot c}{L}\right)^2 - 1\right) \tag{5.3}$$

The error on m^2 can be calculated assuming the error on the flight pass L can be neglected;

$$\sigma_{m^2}^2 = \frac{\sigma_\alpha^2}{K_1^2}(4m^4p^2) + \frac{\sigma_{ms}^2}{K_1^2}\left(4m^4\left(1 + \frac{m^2}{p^2}\right)\right) + \frac{\sigma_{TOF}^2 c^2}{L^2}(4p^2(m^2 + p^2)) \tag{5.4}$$

Where the constant K_1 is the amount of kick the particle gets from the magnetic field and is equal to 87.3 mrad GeV$/c$. Equation 5.4 has included three resolution terms, which are;

- σ_α : Angular resolution $\approx$ 3.0 mrad.

- σ_{ms} : Multiple scattering effect $\approx$ 0.6 mrad.

- σ_{TOF} : Time-of-Flight resolution $\approx$ 115 ps.

Fig. 5.2 shows 2.5 sigma cut for each particle species.

5.3   Event Selection

In this thesis, we have used micro-DSTs(version $03 - 1$), which produced from Data Summary Tapes(DSTs). DSTs include all the reconstructed tracks and their detector-associated quantities.

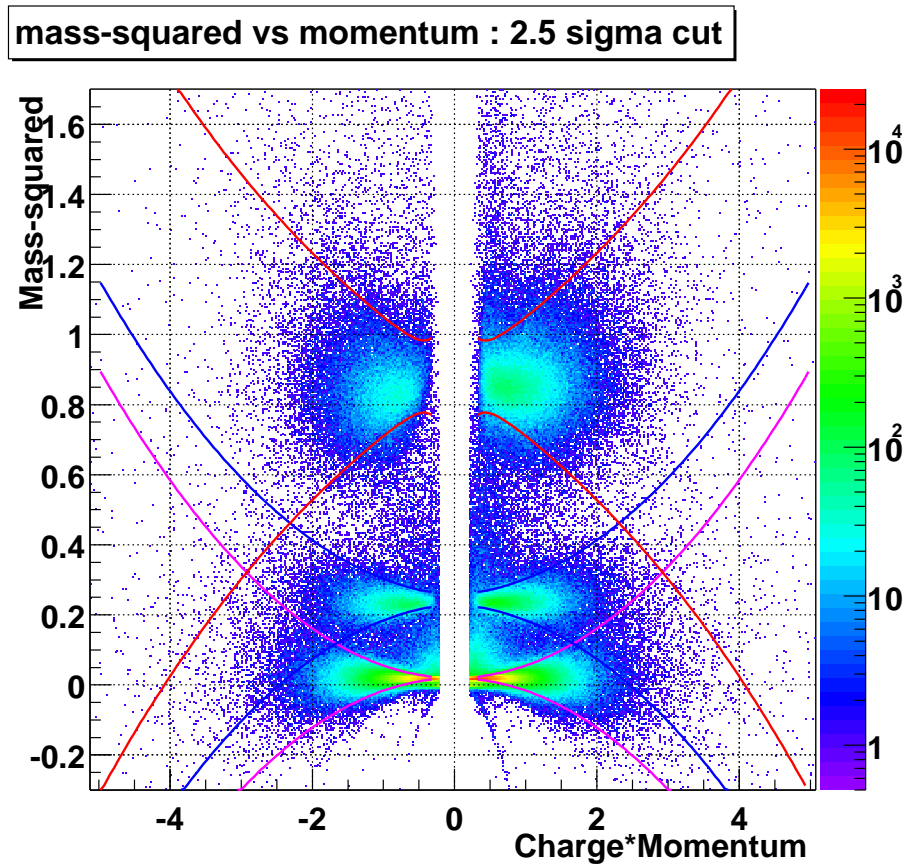For azimuthal anisotropy analysis, we have applied following event selection.

Fig. 5.2: Mass square vs Momentum distribution. 2.5 sigma cut have been applied.

- Used only the PHENIX central magnet ON data.

- Collision vertex cut is applied $| \, Vertex \, | < 20cm$ decided by BBC.

- Track quality factor is larger than 20, which mean that only use track having 3-dimensional information.

- Select particles $0.2GeV < p_t < 2.5GeV$

- Number of tracks > 3 in each sub-events(Description about sub-events is given in 6.1.4)

- Number of DCH tracks and number of PC1 hits correlation cut. To select runs with good conditions of DCH, number of DCH tracks and number of PC1 hits required to be within a given range as shown Fig. 5.3

Applying these cut, about 700K events have been selected for further analysis.
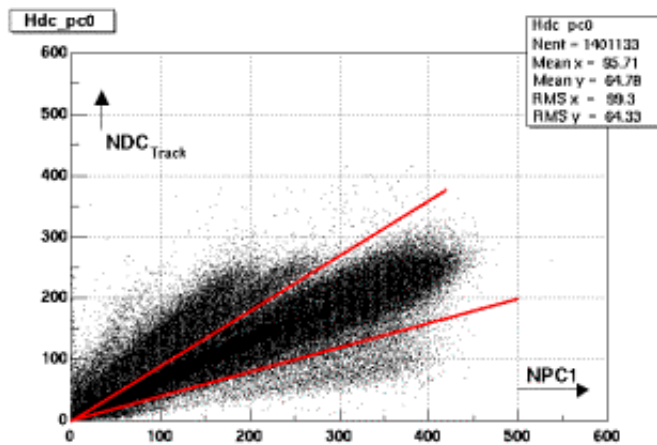

Fig. 5.3: Number of DCH tracks and number of PC1 hits correlation cut. Only use events between red lines.

And for identified particle analysis, following selections have been applied

- $| \, m^2_{measured} - m^2_0 \, | < 2.5\sigma$

- $0.2 < p_t < 2.0$ GeV/c for $\pi+, \pi-$.

- $0.2 < p_t < 2.0$ GeV/c for $K+, K-$.

- $0.2 < p_t < 4.0$ GeV/c for $Proton, \bar{P}$.

In the particle identification, there are some contaminations between pion and Kaon. The ratio of (Contaminated candidates)/(all pion candidates) is about 0.1%. All contaminated candidates are assigned as pion.

6 Experimental Results

6.1 Reaction Plane

The reaction plane calculation using the elliptic component of azimuthal anisotropy has been done with following precedures.

6.1.1 Reaction Plane Determination and Flattening

At first, we should decide reaction plane using charged particles from the PHENIX central arm. The reaction plane has been determined by following expression with p_t as a weight of each particle. Since it is known the anisotropy is larger for larger p_t, therefore the better resolution is expected.

$$2\Psi_0^{obs} = \arctan\left(\frac{\sum_{i=0}^{N} p_{t_i}\sin(2\phi_i)}{\sum_{i=0}^{N} p_{t_i}\cos(2\phi_i)}\right) \tag{6.1}$$

where Ψ_0 is azimuthal angle of reaction plane, ϕ_i is the azimuthal angle of each reconstructed track. In order to correct the effect of limited acceptance of the PHENIX detector, we have adopted correction method called as "flattening method" which is one of the "shifting method" [1]. Correction factor can be obtained next expression;

$$\Delta\Psi_0 = \sum_n (A_n\cos(2n\Psi_0^{obs}) + B_n\sin(2n\Psi_0^{obs})), \tag{6.2}$$

$$A_n = -\frac{2}{n}\langle\sin(2n\Psi_0^{obs})\rangle \tag{6.3}$$

$$B_n = \frac{2}{n}\langle\cos(2n\Psi_0^{obs})\rangle \tag{6.4}$$

where n is degree of Fourier expansion, and n runs up to 100 in this analysis. Note that the bracket $\langle\rangle$ indicates an average over all particles in all sub-events which is used to calculate the reaction plane. The method of sub-events will be discussed
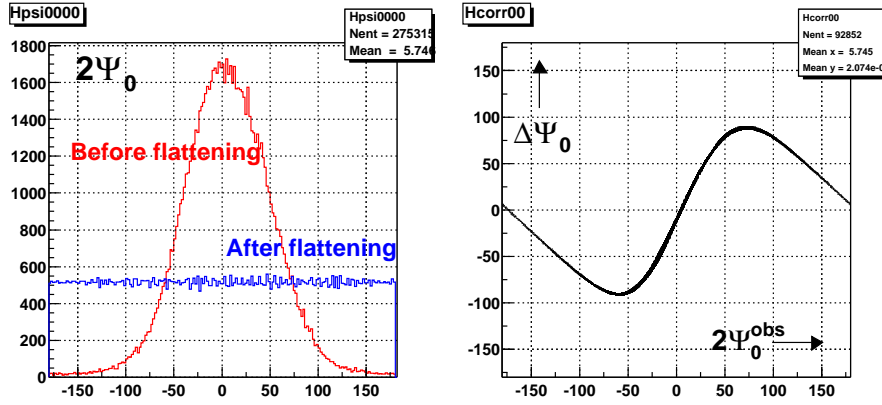
Fig. 6.1: Left:Reaction plane distributions before(red) and after(blue) the flattening correction. Right:Correction factor.

in the following section. The correction factor, $\Delta\Psi_0$, is applied to the observed reaction plane as

$$2\Psi_0 = 2\Psi_0^{obs} + \Delta\Psi_0 \tag{6.5}$$

Fig. 6.1 shows the reaction plane distribution before and after flattening correction, and the flattening correction factor, $\Delta\Psi_0^{obs}$.

6.1.2 Reaction Plane Resolution

Resolution of reaction plane determination is one of the key issues of this methods. In this section we describe the estimation method of resolution.

Here, we define $\Psi_{measured}$ as the measured Ψ_0 and we compare with the true Ψ_0 which is defined as Ψ_{real}. Due to finite resolution in $\Psi_{measured}$, the measured magnitude of the emission pattern would be smaller than the true value.

we consider the azimuthal distribution of the global observable G (as discussed in Section 2.3) Theoretically, the azimuthal distribution of G is given as

$$\begin{aligned}
\frac{dG}{d\phi} &= \frac{G}{2\pi}(1 + \sum_{n=1}^{N} 2v_n \cos(n\phi)) \\
\phi &= \phi_{lab} - \Psi_{real}
\end{aligned} \tag{6.6}$$

where ϕ_{lab} is the measured azimuthal angle of G. Experimentally, the azimuthal distribution of G is obtained by

$$\frac{dG}{d\phi'} = \frac{G}{2\pi}(1 + \sum_{n=1}^{N} 2v'_n \cos(n\phi'))$$ (6.7)

$$\phi' = \phi_{lab} - \Psi_{measured}$$

The relation between v_n and v'_n can be derived as,

$$
\begin{aligned}
v'_n &= \frac{\langle G\cos(n\phi')\rangle}{G/2\pi} \\
&= \frac{\langle G\cos(n\phi)\cos(n(\Psi_{measured} - \Psi_{real}))\rangle}{G/2\pi} \\
&+ \frac{\langle G\sin(n\phi)\sin(n(\Psi_{measured} - \Psi_{real}))\rangle}{G/2\pi} \\
&= \frac{\langle G\cos(n\phi)\rangle\langle\cos(n(\Psi_{measured} - \Psi_{real}))\rangle}{G/2\pi} \\
&= v_n\langle\cos(n(\Psi_{measured} - \Psi_{real}))\rangle
\end{aligned}
$$ (6.8)

The term $\langle G\sin(n\phi)\sin(n(\Psi_{measured} - \Psi_{real}))\rangle$ vanishes because of the reflection symmetry of the ϕ_{lab} distribution with respect to Ψ_0 . Therefore, we can unfold the finite resolution for the Fourier coefficients by dividing the measured Fourier coefficients by the event-averaged mean cosine value of the difference between $\Psi_{measured}$ and Ψ_{real};

$$v_n = \frac{v'_n}{\langle cos(n\Delta\Psi_{measured})\rangle}$$ (6.9)

$$\Delta\Psi_{measured} = \Psi_{measured} - \Psi_{real}$$ (6.10)

In order to evaluate the resolution, sub-events analysis has been adopted. Each event is divided into 2 sub-events A and B . In each sub-event, the reaction plane is determined as Ψ_A and Ψ_B accordingly.

$$
\begin{aligned}
\langle\cos(n(\Psi_A - \Psi_B))\rangle &= \langle\cos(n((\Psi_A - \Psi_{real}) - (\Psi_B - \Psi_{real}))) \\
&= \langle\cos(n(\Psi_A - \Psi_{real}))\rangle\langle\cos(n(\Psi_B - \Psi_{real}))\rangle \\
&+ \langle\sin(n(\Psi_A - \Psi_{real}))\rangle\langle\sin(n(\Psi_B - \Psi_{real}))\rangle \\
&= \langle\cos(n(\Psi_A - \Psi_{real}))\rangle\langle\cos(n(\Psi_B - \Psi_{real}))\rangle
\end{aligned}
$$ (6.11)

The sine term vanishes because of same reason discussed above. From Equation 6.11, the fluctuation of the angle around Ψ_{real} is estimated by (if resolution of each sub-event is expected to be the same)

$$\langle\cos(n(\Psi_A - \Psi_{real}))\rangle = \sqrt{\langle\cos(n(\Psi_A - \Psi_B))\rangle} \tag{6.12}$$

The resolution corrections of measured Ψ_0 for the full size events are obtained by correcting for the fact that the full events have twice the multiplicity of the sub-events considered. When the resolution corrections are small compared to 1, this can be done by multiplying the resolution correction by $\sqrt{2}$;

$$\langle\cos(n\Delta\Psi_{measured})\rangle \approx \sqrt{2} \cdot \sqrt{\langle\cos(\Psi_A - \Psi_B)\rangle} \tag{6.13}$$

6.1.3 Evaluate the strength of azimuthal anisotropy

When reaction plane resolution is obtained, strength of azimuthal anisotropy can be evaluated by fitting of $\phi - \Psi_0$ distribution in terms of the Fourier expansions;

$$f(\phi) = N_0(1 + 2v_2^{obs}\cos(2(\phi_i - \Psi_0))). \tag{6.14}$$

Alternatively, numerical evaluation of v_2^{obs} can be done by;

$$v_2^{obs} = \langle\cos(2(\phi_i - \Psi_0))\rangle. \tag{6.15}$$

While these two methods give the same results within statistical errors, we have adopted the numerical method in this analysis. Finally, the observed strength of v_2^{obs} is corrected by the resolution of reaction plane as described equation 6.12;

$$v_2 = \frac{v_2^{obs}}{Resolution} \tag{6.16}$$

6.1.4 Sub-events

There are many ways to create sub-events. Comparisons of results from different sub-event analysis might provide good systematic check and stability test. Clues of other sources of azimuthal correlations might be obtained as well. In this analysis, we have applied 5 different kinds of sub-events selections.

- ϕ-slice: Divide the acceptance in ϕ into 50 bins with a gap 0.2 degree in between. Gap is implemented in order to avoid auto-correlation.

- η-slice: Divide the η acceptance into 20 bins with a gap 0.01 in between.

- Random: Randomly selected into 2 groups.

- Charge: Each group is created by same charged particles.

- ϕ-slice without p_t weight: Divide ϕ into 50 bins, and determine the reaction plane without p_t weight.

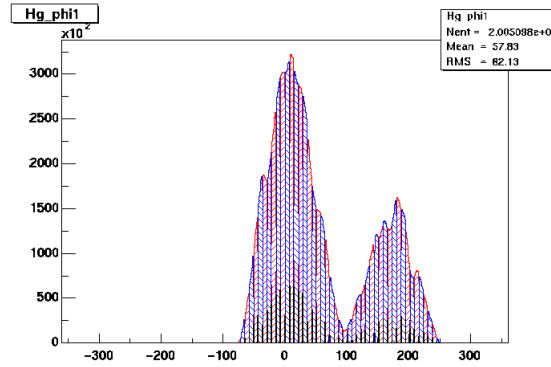Fig. 6.2 and Fig. 6.3 show the results of ϕ-slice,η-slice group selection.

Fig. 6.2: ϕ-slice group selection. Two colors(red and blue) show the two groups(A and B). Black hatched region is gap.
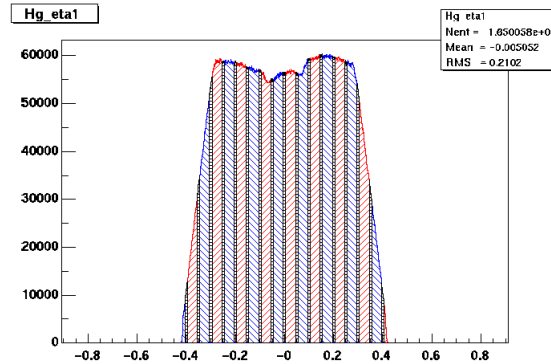

Fig. 6.3: η-slice group selection. Two colors(red and blue) show the two groups(A and B). Black hatched region is gap.
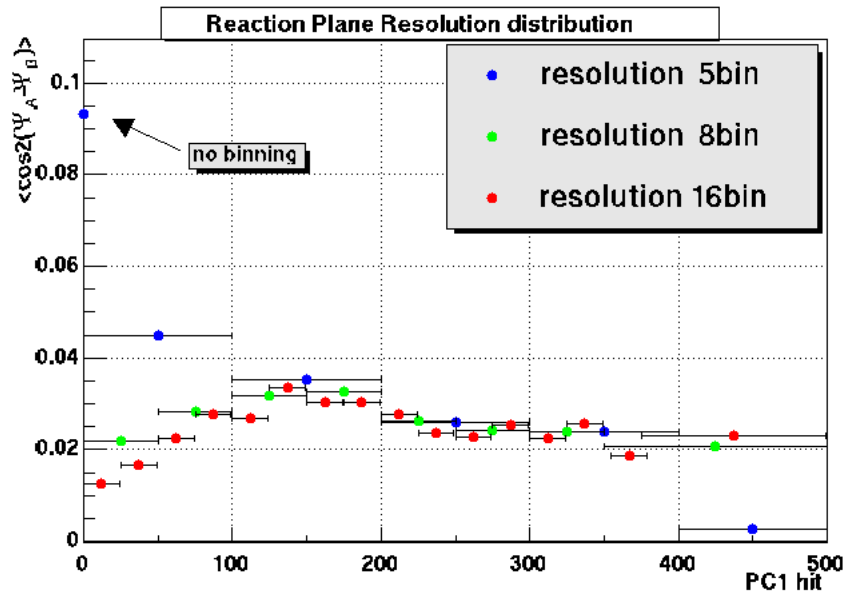
Fig. 6.4: Multiplicity dependence of reaction plane resolution.

6.1.5 Multiplicity Dependence of Reaction Plane Resolution

Fig. 6.4 shows the PC1 multiplicity dependence of reaction plane resolution. Three symbols in the figure indicate the resolution for the different bin sizes in PC1 multiplicity. There is a big difference at the low multiplicity, which is caused by that the shape of reaction plane distribution before the flattening correction is a strong function of the multiplicity as shown in Fig. 6.5

The reason is that averaging of the different reaction plane distribution in one multiplicity bin and making one correction factor by flattening method give us the flat reaction plane in average in the bin, however for each different reaction plane distributions for each multiplicity in the bin it's not flat at all even after the flattening, which always increases the value artificially. An extrema case is shown as a blue dot on the y-axis in Fig. 6.4, where there is only one bin for all PC1 multiplicity. The value reduces with increasing the number of bins in the multiplicity. Fig. 6.6 shows 16 bins of PC1 multiplicity used in this analysis.
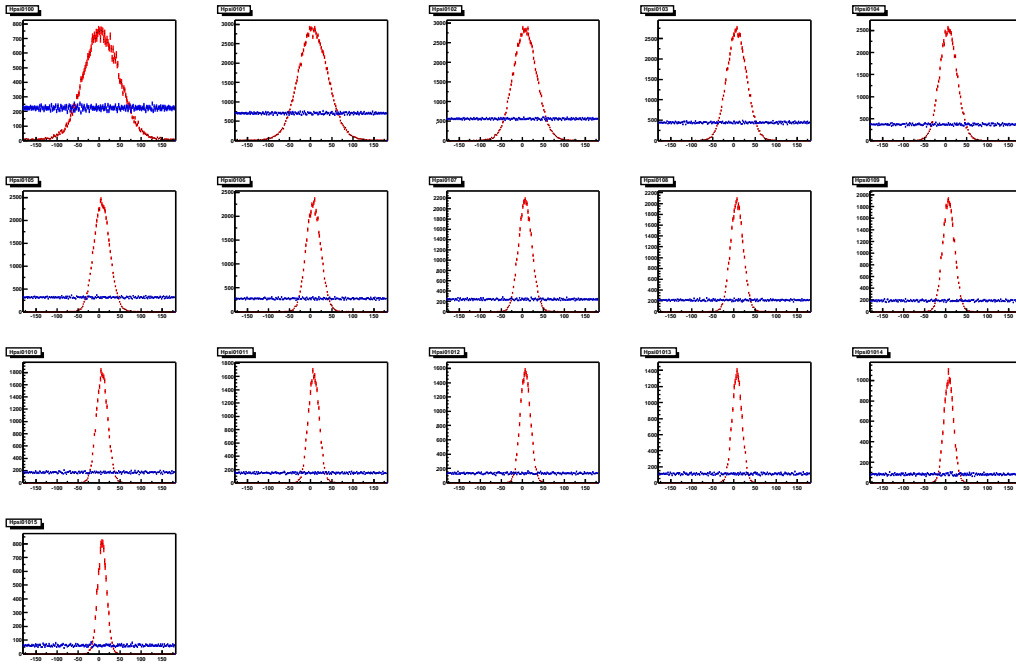
Fig. 6.5: Reaction plane distributions multiplicity bin by bin. From top-left to bottom-right, the PC1 multiplicity is $(0)0 - 25, (1)25 - 50, (2)50 - 75, (3)75 - 100, (4)100 - 125, (5)125 - 150,$ $(6)150 - 175, (7)175 - 200, (8)200 - 225, (9)225 - 250, (10)250 - 275,$ $(11)275 - 300, (12)300 - 325, (13)325 - 350, (14)350 - 375, (15)375 <,$ respectively. The red curves are reaction plane distribution before flattening correction, and the blue ones are after correction.

Number of PC1 hits

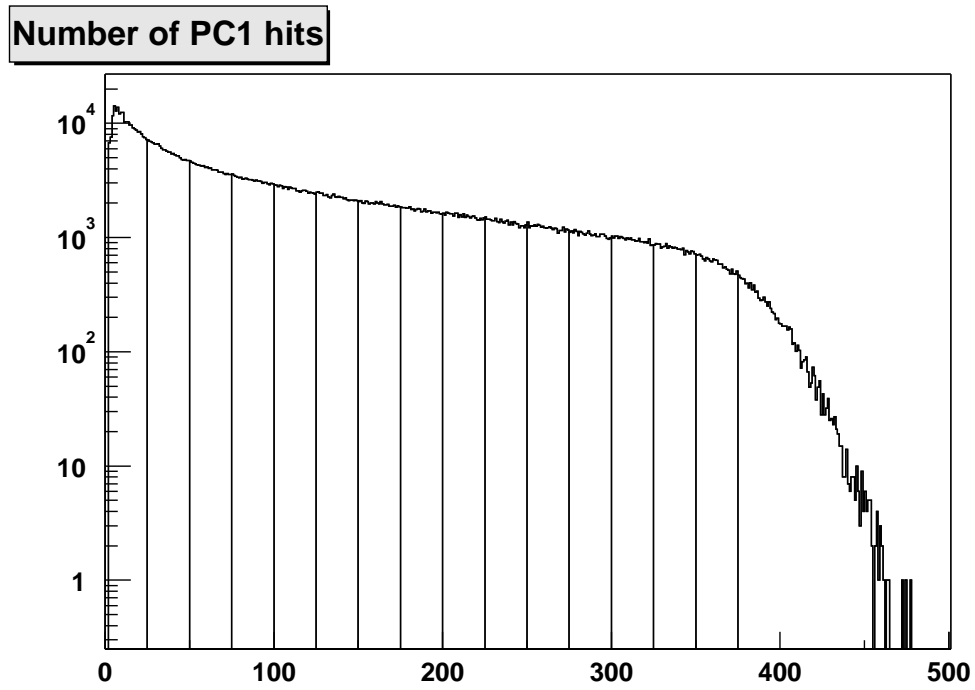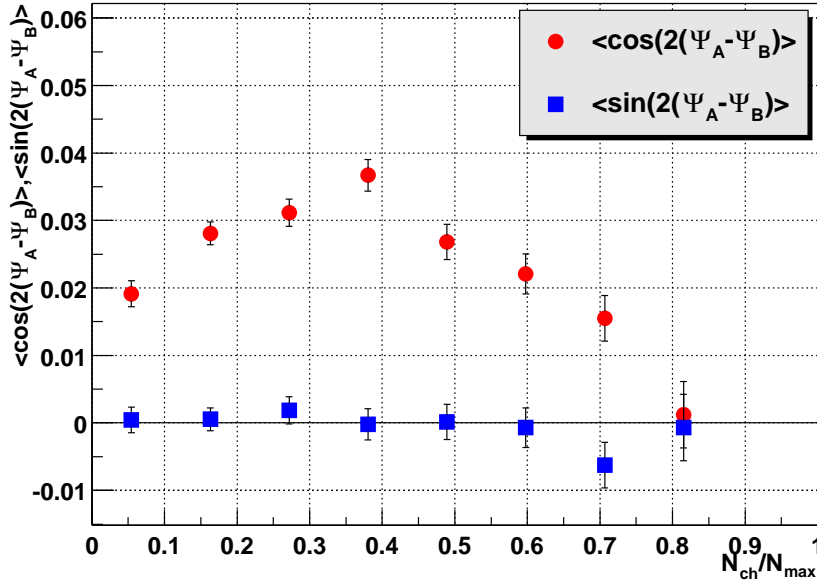Fig. 6.6: The PC1 multiplicity distribution. The 16 multiplicity bins used in this analysis are shown.

Fig. 6.7: The $\langle\cos(2(\Psi_A-\Psi_B))\rangle$ and the $\langle\sin(2(\Psi_A-\Psi_B))\rangle$ distributions as a function of normalized PC1 multiplicity. The sub-events selection is "ϕ-slice".

6.1.6   Reaction Plane Resolution Distribution

As described in 6.1.2, the reaction plane resolution is estimated by averaging the $\cos(\Delta\Psi_0)$, where the $\Delta\Psi_0$ is the angular difference between the reaction planes from the 2 sub-events. Fig. 6.7 shows reaction plane resolution which is plotted as a function of PC1 the multiplicity normalized by the maximum observed number of hits. The $\langle\cos(2(\Psi_A - \Psi_B))\rangle$ is the largest at the semi-central region, where the resolution is the best. This shape is explained by the small elliptic emission at the central region and the less number of tracks at the peripheral region. The $\langle\sin(2(\Psi_A - \Psi_B))\rangle$ should be zero, because the $(\Psi_A - \Psi_B)$ distribution is an even function, and it has been confirmed to be zero.

6.2 Azimuthally Correlations between Observed Charged Particles and Reaction Plane

Fig. 6.8 shows the difference of ϕ and Ψ_0, that is, the correlation between the corrected reaction plane angle, and the measured azimuthal angle of all charged particles in different multiplicity regions. Clear amplitude increase of azimuthally correlations is shown from central to peripheral.
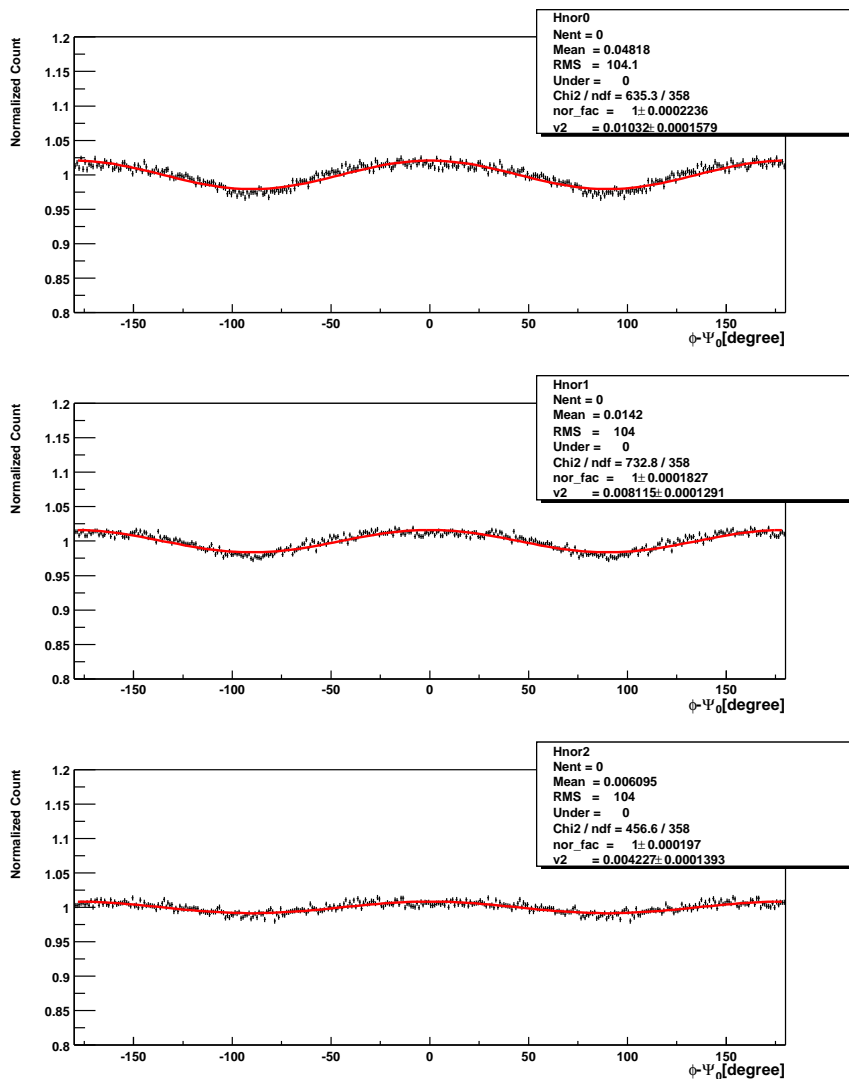

Fig. 6.8: $\phi - \Psi_0$ distributions for three multiplicity ranges. From top to bottom, multiplicity range is 0-125, 125-250, 250-460, respectively.

6.3   Azimuthal Anisotropy of Charged Particle Emission

6.3.1   Multiplicity Dependence of v_2

Multiplicity dependence of v_2 parameters that have already been corrected by the reaction plane resolution is shown in Fig. 6.9. 5 different kinds of sub-event results are shown in the plot. There is a clear multiplicity dependence of v_2, and v_2 is the largest at the most peripheral collision region. The results of the different sub-events methods agree well in spite of the fact that resolution distributions are in broad range as shown in Fig. 6.10

However, η-slice sub-event result is slightly small. There should be other sources of azimuthal correlations such as, Jets, HBT correlation, resonance decay, momentum conservation which could be different for the different sub-events.
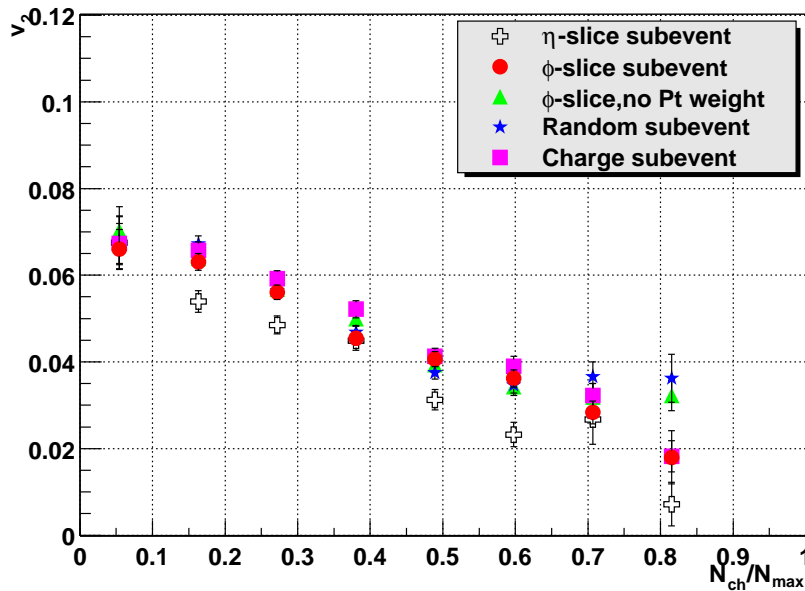

Fig. 6.9: Multiplicity dependence of v_2 for different kinds of sub-events selection.

6.3.2   Systematic Error Estimation

To estimate systematic error of this analysis, we have been used the results of multiplicity dependence for different sub-events methods which is shown previous
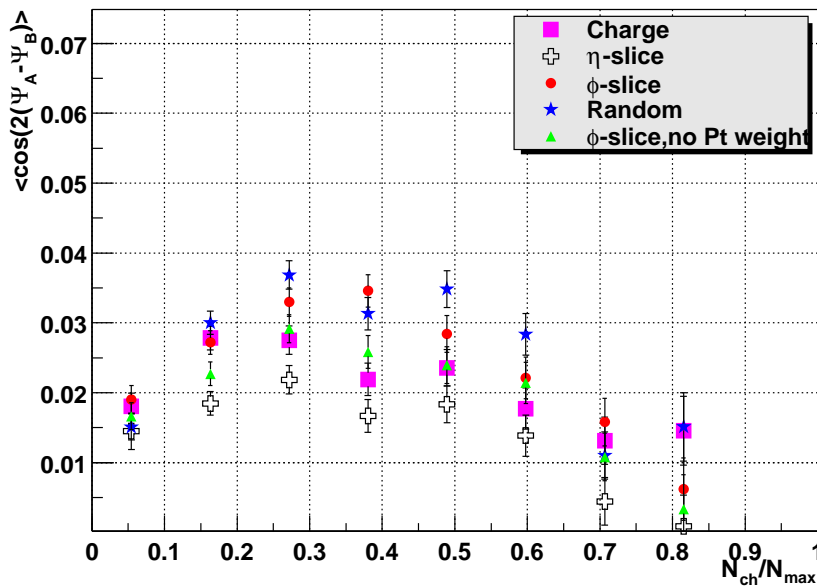
50

Fig. 6.10: Reaction plane resolution distribution for all sub-events selection.

section. At present, assuming that other source of azimuthal correlations is not so large, we define the difference of the value from the different sub-events selections as the systematic error. Fig. 6.11 shows the relative difference of the different sub-events compared to the ϕ-slice sub-event selection. (and it's normalized to the ϕ-slice sub-event selection.) The largest difference is used as the systematic error in this analysis. The systematic uncertainty is about 5% at most peripheral bin, 100% at most central bin.

Fig. 6.12 shows multiplicity dependence of v_2 which includes both systematic and statistical errors. (This systematic analysis is still in preliminary.)

6.3.3 p_t Dependence of v_2

Fig. 6.13 shows the transverse momentum dependence of v_2. The elliptic emission strength increase with larger p_t and saturate at larger p_t.
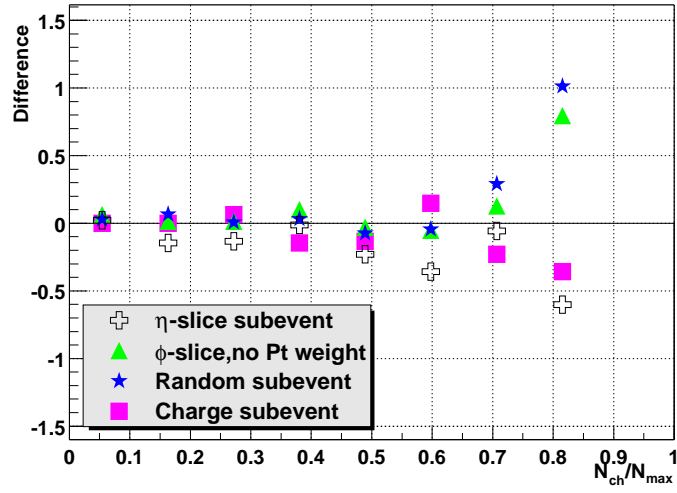
Fig. 6.11: The relative difference of v_2 parameters for different sub-event selection.
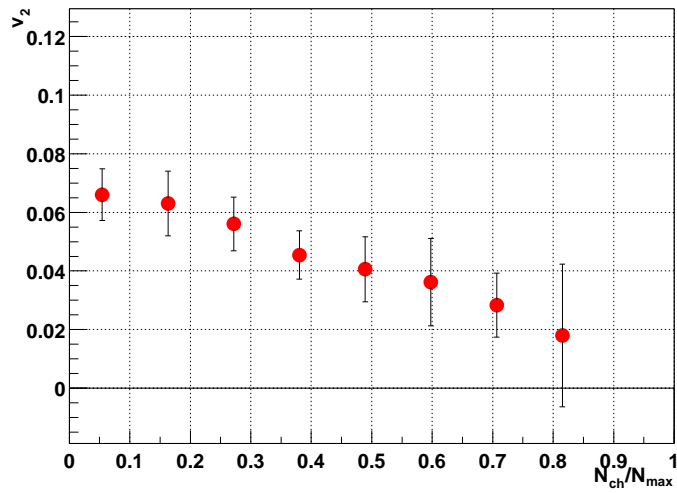

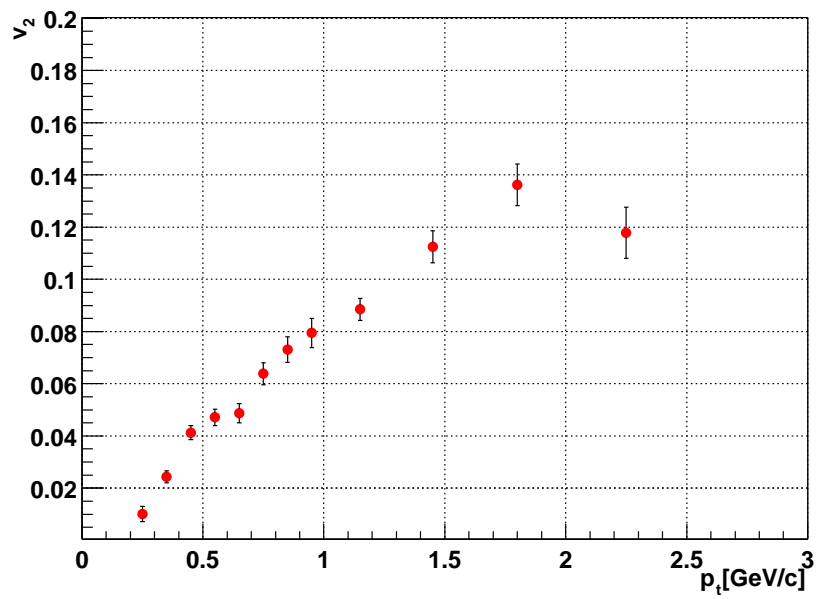Fig. 6.12: Multiplicity dependence of v_2 with systematic and statistical errors.

Fig. 6.13: Transverse momentum dependence of v_2. Error bars only include statistical error.

6.4 Azimuthally Correlations between Observed Identified Particles and Reaction Plane

Fig. 6.14 shows the $\phi - \Psi_0$ distribution for different particle species. (The cut range for each particle is described in Sec.5.3.) Multiplicity, η and p_t is integrated. The anisotropy of azimuthal correlation for identified particle is shown.
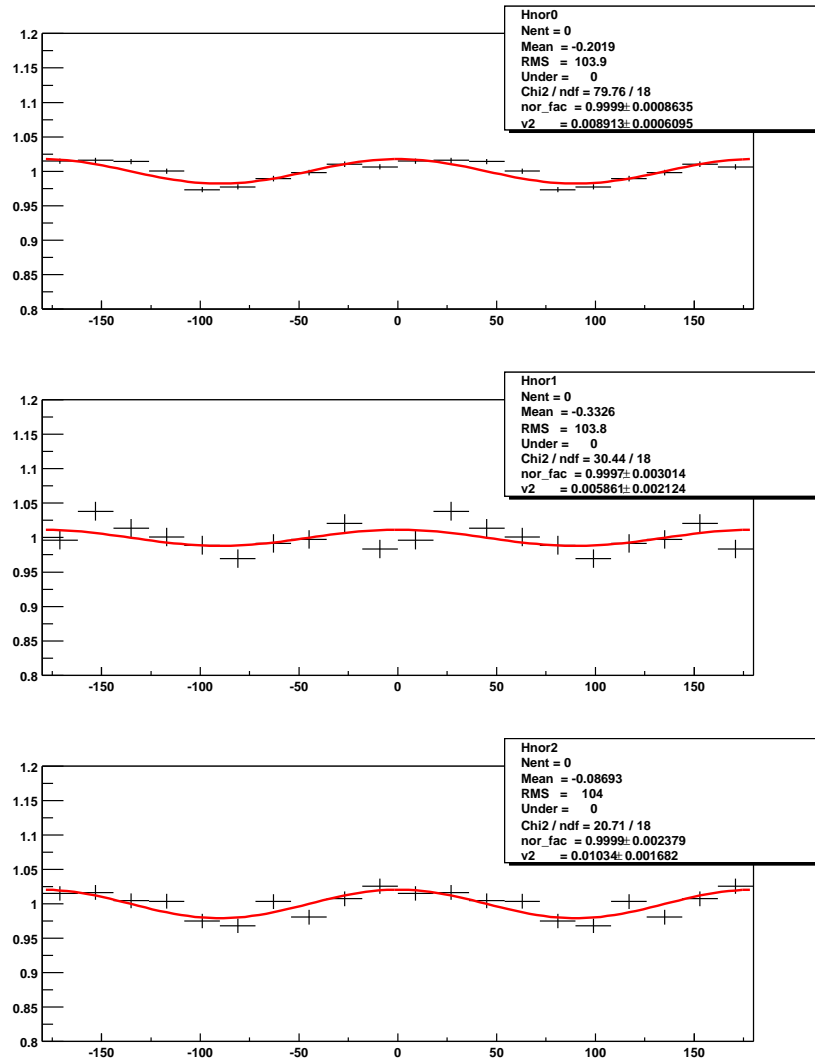

Fig. 6.14: $\phi - \Psi_0$ distributions for identified particle. From top to bottom, $\pi^+ + \pi^-$, $K^+ + K^-$ and $Proton + Pbar$.

6.5 Azimuthal Anisotropy of Identified Particle Emission

6.5.1 Mass Dependence of v_2

After resolution correction, particle mass dependence of v_2 is obtained. v_2 is plotted as a function of particle mass in Fig. 6.15 . It seems that v_2 of proton and pbar is greater than pion's one, which is predicted hydro-dynamical calculation [23]. v_2 values of Kaon and pion are same within statistical error.
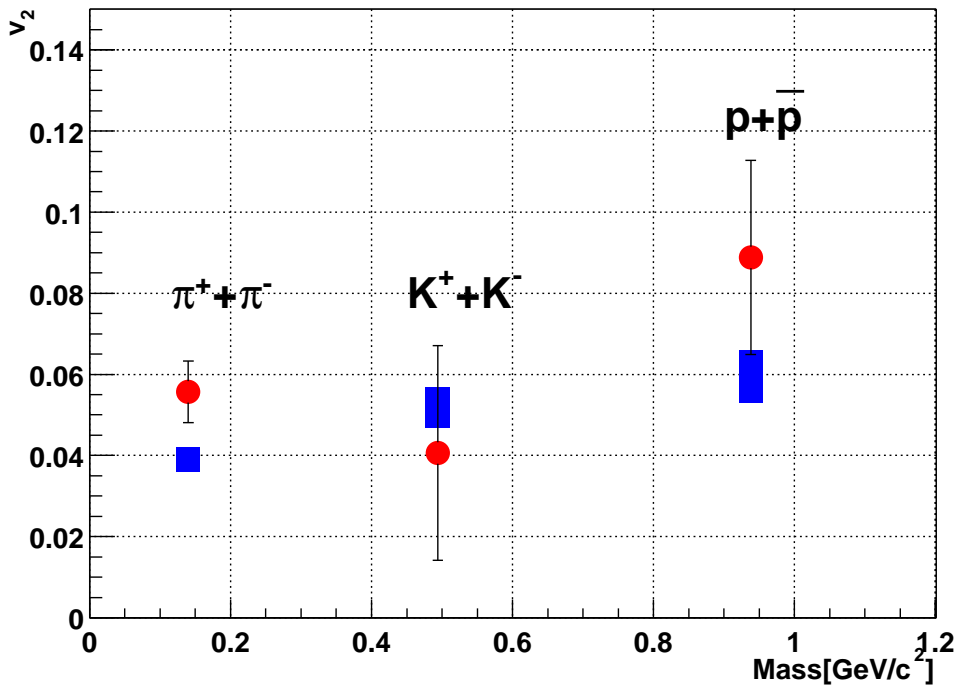

Fig. 6.15: Mass dependence of v_2. Solid squares are hydro-dynamical prediction [23]. Error bar is statistical only.

6.5.2 Multiplicity Dependence of v_2

Fig. 6.16 and Fig. 6.17 shows PC1 multiplicity dependence of identified particle's elliptic emission pattern strength. The multiplicity dependence seem to be visible for each particles.

Fig. 6.16: Mass and multiplicity dependence of v_2 value for *Plus* charged particle. Red circle indicate central($0.43 < n_{ch}/n_{max}$) collision region, and blue one indicate peripheral ($n_{ch}/n_{max} < 0.43$) collision region. From left to right, the data indicate $\pi+$, $K+$ and *Proton*. Error bar is statistical only.
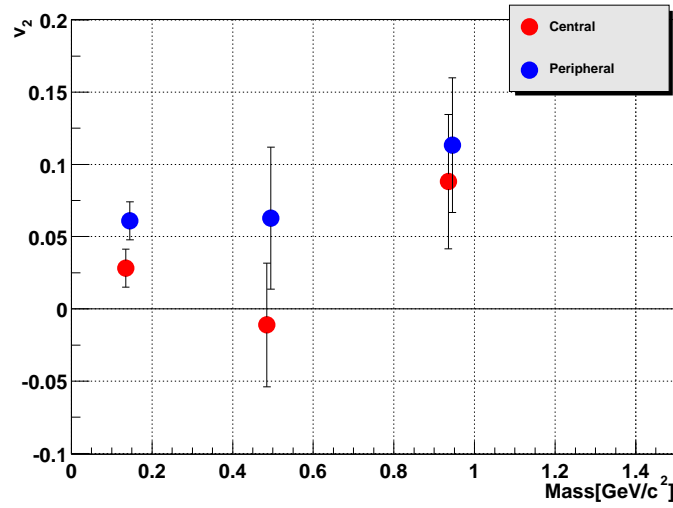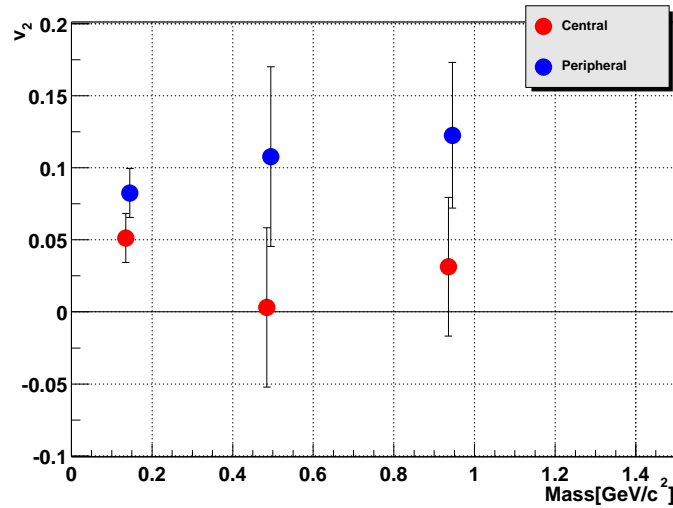

Fig. 6.17: Mass and multiplicity dependence of v_2 value for *Minus* charged particle. Red circle indicate central($0.43 < n_{ch}/n_{max}$) collision region, and blue one indicate peripheral ($n_{ch}/n_{max} < 0.43$) collision region. From left to right, the data indicate $\pi-$, $K-$ and *Pbar*. Error bar is statistical only.

7 Discussion

In this section, we compare the experimental results with an "Two Particle Azimuthal Correlation Method" and the other experimental results.

7.1 Comparison with Other Measurement

Fig. 7.1 shows the comparison the experimental results with "Two Particle Azimuthal Correlation Method" and the results of the STAR experiment as well. Different method results("Two Particle Azimuthal Correlation Method" and "Reaction Plane Method") and the STAR result have a good consistency.

Fig. 7.2 shows the comparison with STAR and PHOBOS experimental results. Three different experimental results agree well.

From these graphs, "Reaction Plane Method" is available even the detector doesn't have fully azimuthal acceptance such as the PHENIX detector. And the consistency result tells us other sources of azimuthal correlations effects are not so big.
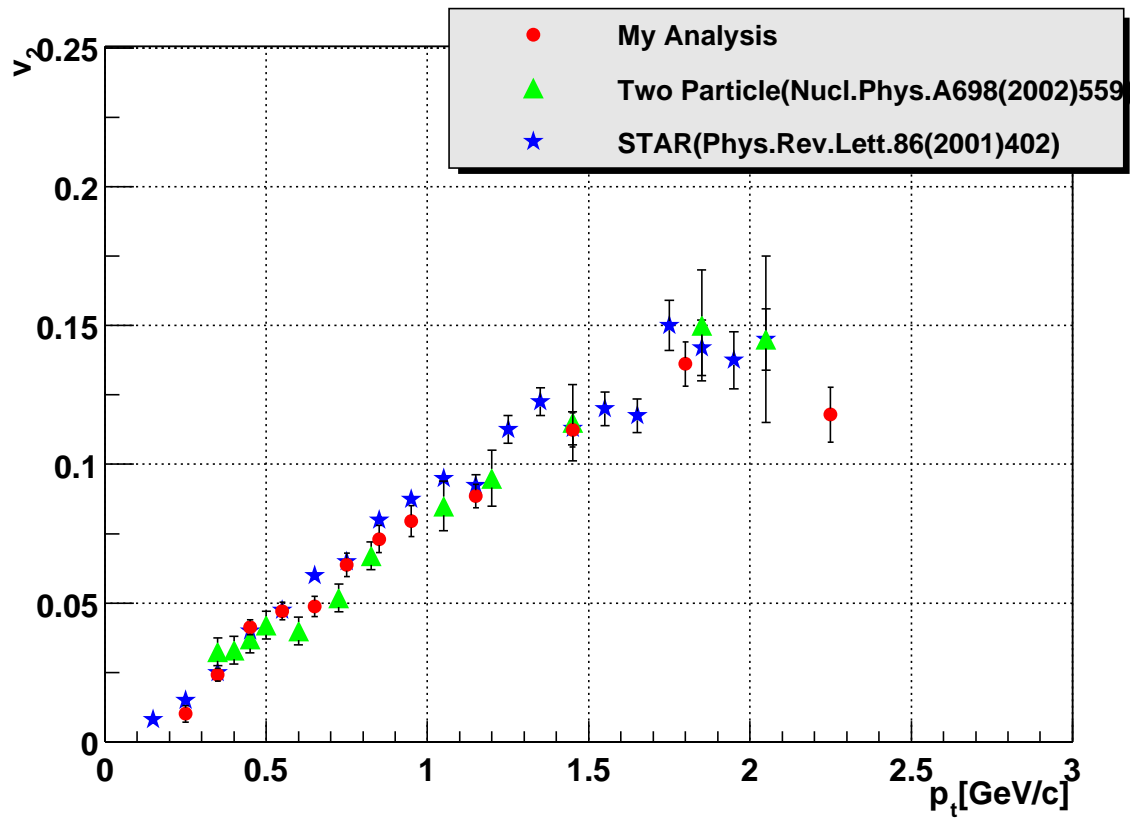
Fig. 7.1: The comparison the experimental result with the "Two Particle Azimuthal Correlation Method" and the STAR published result in p_t dependence of v_2. The results agree well.
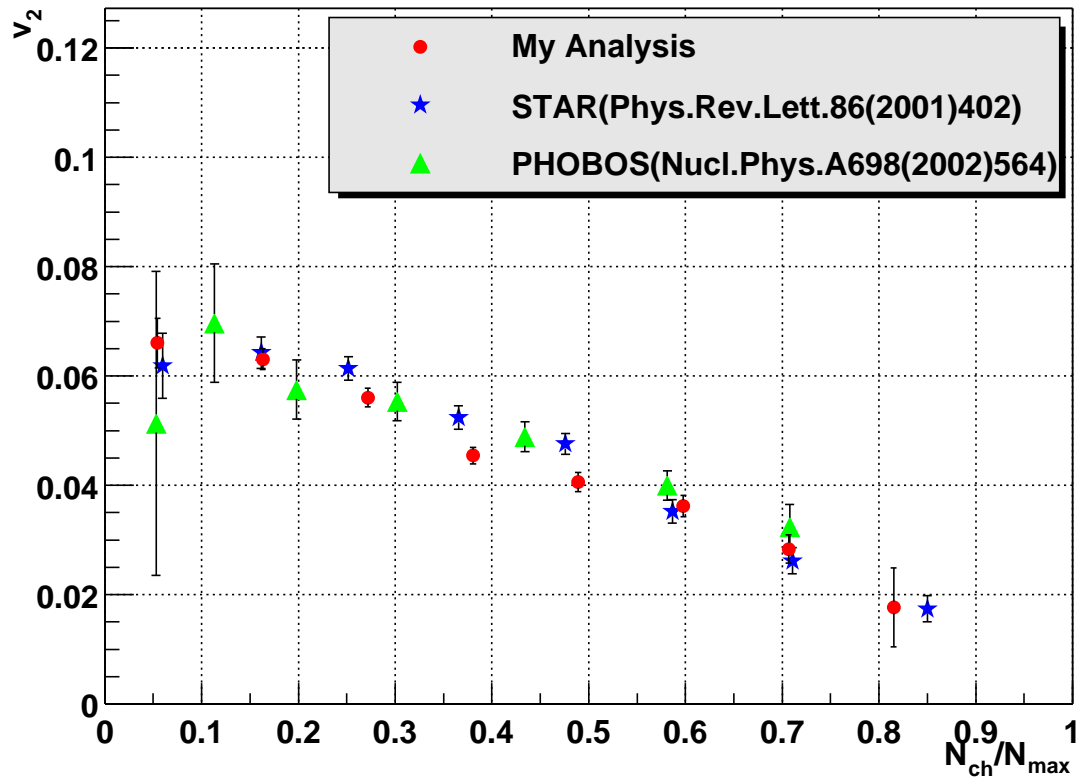
Fig. 7.2: The comparison the experimental result with the STAR and the PHOBOS experimental result in normalized multiplicity dependence of v_2. Different experimental results have a beautiful consistency.

7.2   Incident Energy Dependence of Azimuthal Anisotropy of Particle Emission

Fig. 7.3 shows the compilation of observed v_2 parameters as a function of incident beam energy in laboratory flame. A transition from out-of-plane to in-plane elliptic emission occurs at around 5-10 A GeV. The strength of elliptic emission pattern have been increasing with beam energy.
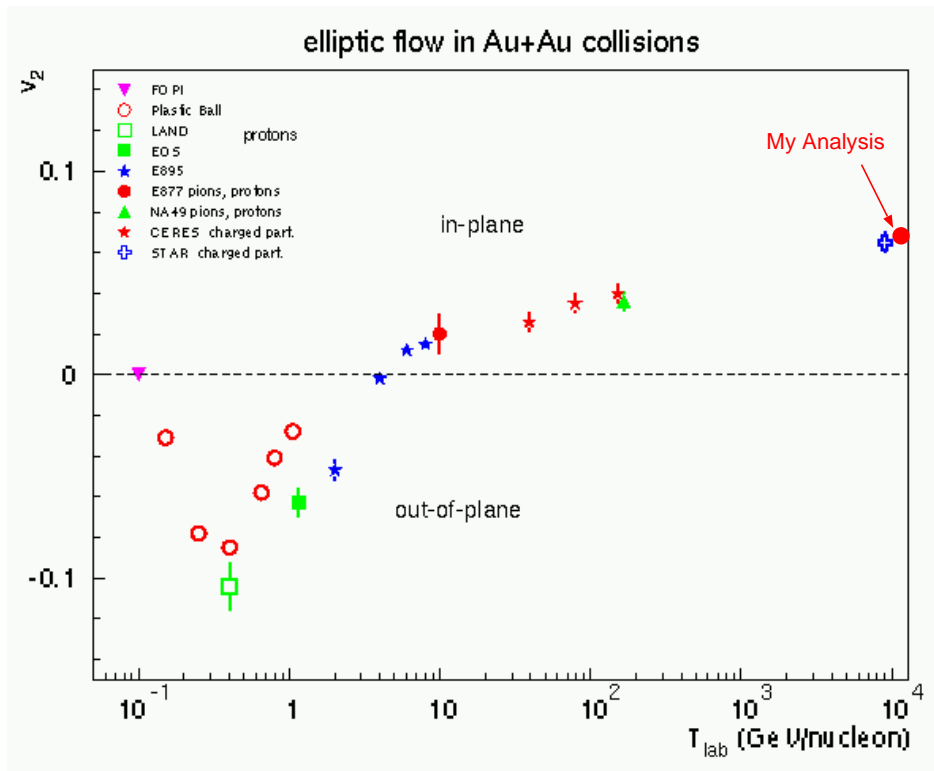
Fig. 7.3: Incident beam energy dependence of v_2 parameters. The data point obtained from this analysis is shown.

8 Conclusions

We have presented the results of azimuthal anisotropy of particle emission in $\sqrt{s_{NN}}$=130 GeV Au + Au collisions at RHIC-PHENIX experiment. To extract azimuthal anisotropy, we have adopted "Reaction Plane Methods" .

We have obtained the following results;

- "Reaction Plane Method" is available even the detector doesn't have a fully acceptance such as the PHENIX detector.

- Reaction plane can be defined using central arm in the PHENIX experiment.

- Different sub-events selection calculations give us consistency results.

- p_t dependence of elliptic emission pattern has a good consistency with "Two Particle Azimuthal Correlation Methods" and the STAR experiment results.

- Multiplicity dependence of elliptic emission pattern agree well the STAR and the PHOBOS experiment results.

- Consistent results between 2 different analysis methods say that other sources of azimuthal correlations effects might be small.

- A elliptic emission pattern of identified particle have been measured, and the mass dependence has a hydro-dynamic behavior.

The results indicate that we have good opportunity to study azimuthal anisotropy of particle emission and its systematic uncertainty using various analysis methods. We will be able to measure the identified particle's azimuthal anisotropy with more statistical after Year-2 experiment at RHIC-PHENIX.

Acknowledgments

A   Simulation Study of Azimuthal Anisotropy Analysis Including Extreme Jets Component

Purpose

The main purpose of this simulation is to estimate the jets contributions in the azimuthal anisotropy analysis.

Simulation

We have generated "Extreme" jets as follows;

- Number of generated tracks in each event are 500 with elliptic emission $v_2 \approx 6\%$.

- Number of generated jets tracks are 10% of all tracks(=50) in one set of back to back jet cones.

- The cone including jets is *Gaussian* distribution with sigma of 1.7,5.7 and 17 degree.

- Jets angle is random with respect to the elliptic emission angle.

- Use "Two Particle Azimuthal Correlation Method" and "Reaction Plane Method" for analysis.

Fig. A.1 shows generated tracks and reconstructed ϕ distributions. When there are very strong jets component, the clear amplitude increase is shown in the $\Delta\phi$ and $\phi - \Psi_0$ distributions.

Fig. A.2 shows rapidity dependence of v_2 parameters. There values are evaluated by $\langle\cos(2x)\rangle$. Both analysis methods give the same results($\approx 10\%$) surprisingly,

64
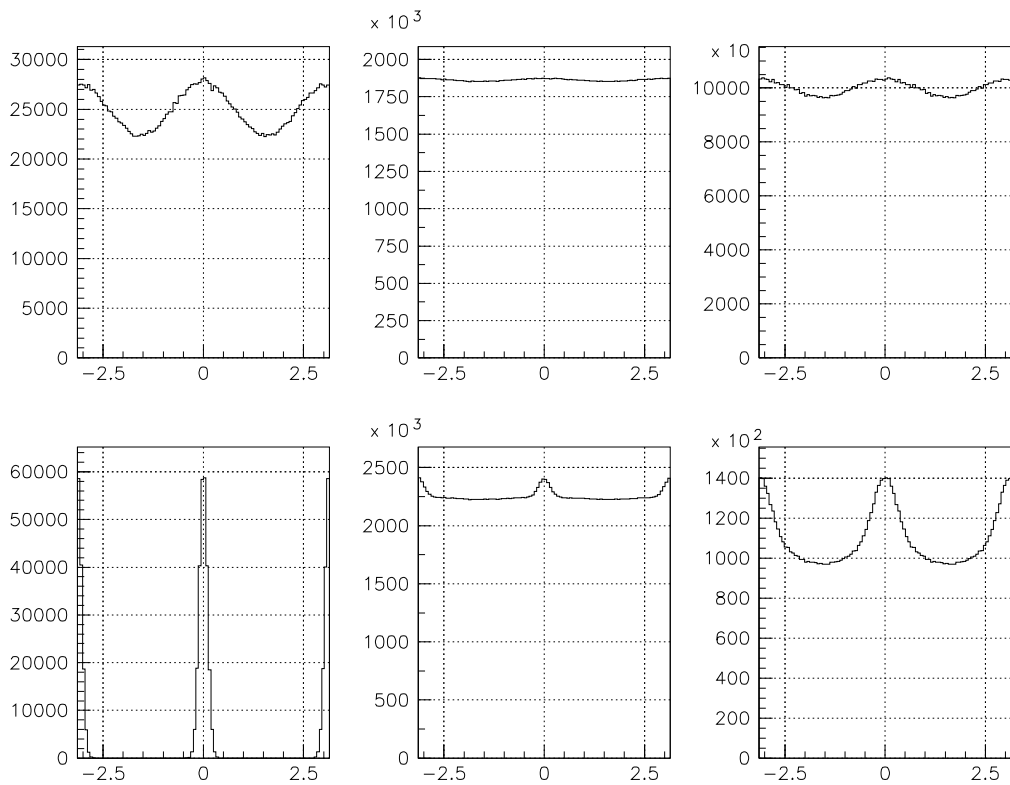
Fig. A.1: Example of simulation; The jets cone size is 5.7degree. Top-left: Generated elliptic emission pattern. Top-middle: $\Delta\phi$ distribution with elliptic emission only. Top-right: $\phi - \Psi_0$ distribution with elliptic emission only. Down-left: Generated jets. Down-middle: $\Delta\phi$ distribution including elliptic emission and jets. Down-right: $\phi - \Psi_0$ distribution including elliptic emission and jets.
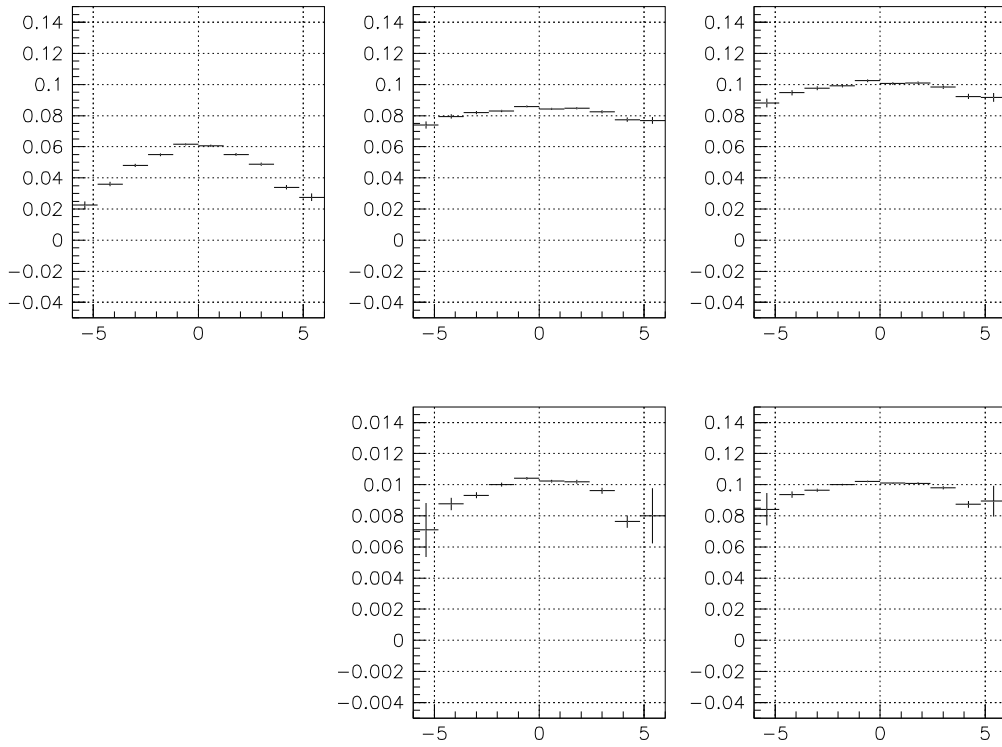
Fig. A.2: v_2 distributions as a function of rapidity. Top-left: Generated v_2 parameters. Top-middle: Reconstructed v_2^{obs} by reaction plane method. Top-right: v_2 parameters after resolution correction. Down-middle: Reconstructed v_2^{obs} by two particle azimuthal correlation method. Down-right: Obtained v_2 parameters by two particle azimuthal correlation method.

although these reconstructed v_2 values are larger than generated values ($\approx 6\%$). Because $\langle \cos(2x) \rangle$ gives only average amplitude of $\Delta\phi$ and $\phi - \Psi_0$ distributions. The left column graphs in the Fig. A.3 shows the $\Delta\phi$ and $\phi - \Psi_0$ distributions fitted by Fourier expansion($F(x) = N_0(1 + 2v_2\cos(x))$). These clearly indicate that $\langle \cos(2x) \rangle$ calculation does not give the correct v_2 value when jets component is large. (Fitting by Fourier expansion and $\langle \cos(2x) \rangle$ calculation are equivalent.)
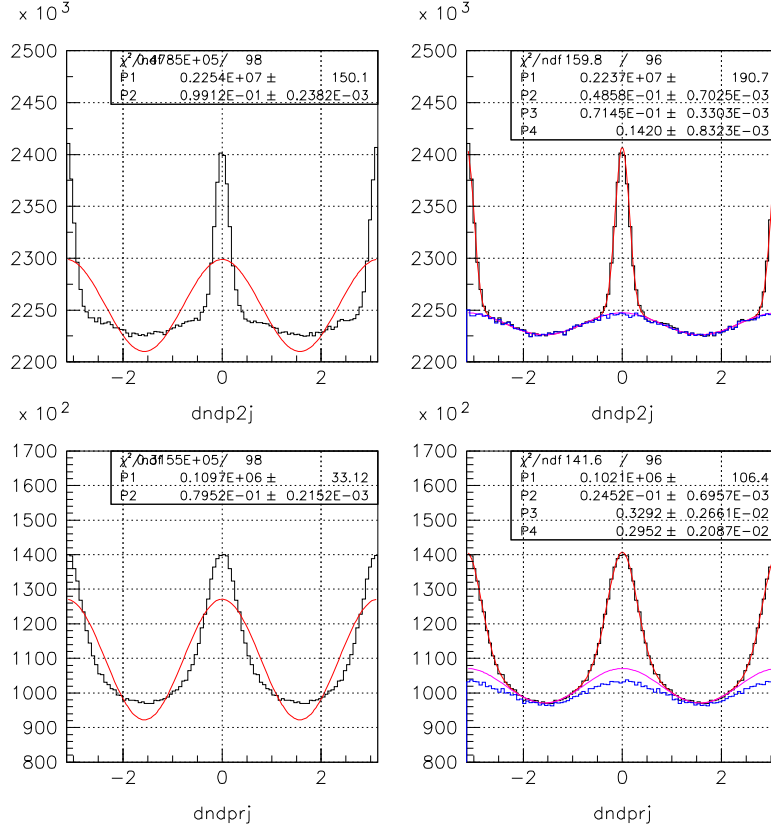
Fig. A.3: Top-left: $\Delta\phi$ distribution fitted by $F(x) = N_0(1 + 2v_2^2\cos(x))$. Top-right: $\Delta\phi$ distribution fitted by $F(x) = N_0(1 + 2v_2^2\cos(x) + Gaussian)$ (Large amplitude). $\Delta\phi$ distribution without jets component (Small amplitude). Down-left: $\phi - \Psi_0$ distribution fitted by $F(x) = N_0(1 + 2v_2'\cos(x))$. Down-right: $\phi - \Psi_0$ distribution fitted by $F(x) = N_0(1 + 2v_2'\cos(x) + Gaussian)$ (Large amplitude). $\phi - \Psi_0$ distribution without jets component (Small amplitude).

We have been also applied following fitting methods;

- Use the function including jets component.
  $F(x) = N_0(1 + 2v_2\cos(x) + Gaussian)$

(Large amplitude histogram in right column in Fig. A.3.)

- After removing jets component from original distributions, apply the Fourier expansion fit $(F(x) = N_0(1 + 2v_2 \cos(x)))$.

The Tab. A.1 and Tab. A.2 show the results.

Size of jets cone [degree]	$\langle\cos(2x)\rangle$ [%]	Fit by cosine+Gaussian [%]	Without jets component [%]
0(no jets)	5.224±0.0495	5.224±0.04962	5.224±0.04943
17	8.889±0.02636	5.416±0.1477	4.75±0.05
5.7	9.915±0.02015	4.856±0.07044	4.75±0.04938
1.7	9.701±0.02186	4.791±0.0542	4.75±0.04911

Tab. A.1: Simulation results using "Two Particle Azimuthal Correlation Method".

Size of jets cone [degree]	$\langle\cos(2x)\rangle$ [%]	Fit by cosine + Gaussian [%]	Without jets component [%]
0(no jets)	5.364±0.0355	5.364±0.0348	5.364±0.0349
17	8.757±0.0271	4.117±0.2532	2.477±0.02832
5.7	9.504±0.02571	2.931±0.0878	2.013±0.02672
1.7	9.554±0.02557	2.867±0.0726	1.964±0.02656

Tab. A.2: Simulation results using "Reaction Plane Method".

Size of jets cone [degree]	$\langle\cos(\Psi_A - \Psi_B)\rangle$
0(no jets)	0.41
17	0.62
5.7	0.70
1.7	0.71

Tab. A.3: Reaction plane resolution for each jets cone size.

The v_2 values obtained by two particle azimuthal correlation method have ± 10 % difference from generated values. v_2 reconstruction by reaction plane method 25∼50 % smaller than generated values. This might be because of following 2 reasons;

- Measured v_2 is affected by the jets.

- Reaction plane can not be determined correctly because of the random jets.

Summary

In extreme situation, there are very strong jets contributions in the azimuthal correlations, both analysis methods can not reconstruct v_2 parameters correctly. When the influence of jets is large, the effect will appear in the $\Delta\phi$ and $\phi - \Psi_0$ distributions which are different from $F(x) = N_0(1 + 2v_2\cos(2x))$ distribution. If these contributions are shown in the real analysis, we should investigate the origin source and consider the proper treatment.

B The PHENIX Collaboration List

K. Adcox,[40] S. S. Adler,[3] N. N. Ajitanand,[27] Y. Akiba,[14] J. Alexander,[27] L. Aphecetche,[34] Y. Arai,[14] S. H. Aronson,[3] R. Averbeck,[28] T. C. Awes,[29] K. N. Barish,[5] P. D. Barnes,[19] J. Barrette,[21] B. Bassalleck,[25] S. Bathe,[22] V. Baublis,[30] A. Bazilevsky,[12,32] S. Belikov,[12,13] F. G. Bellaiche,[29] S. T. Belyaev,[16] M. J. Bennett,[19] Y. Berdnikov,[35] S. Botelho,[33] M. L. Brooks,[19] D. S. Brown,[26] N. Bruner,[25] D. Bucher,[22] H. Buesching,[22] V. Bumazhnov,[12] G. Bunce,[3,32] J. Burward-Hoy,[28] S. Butsyk,[28,30] T. A. Carey,[19] P. Chand,[2] J. Chang,[5] W. C. Chang,[1] L. L. Chavez,[25] S. Chernichenko,[12] C. Y. Chi,[8] J. Chiba,[14] M. Chiu,[8] R. K. Choudhury,[2] T. Christ,[28] T. Chujo,[3,39] M. S. Chung,[15,19] P. Chung,[27] V. Cianciolo,[29] B. A. Cole,[8] D. G. D'Enterria,[34] G. David,[3] H. Delagrange,[34] A. Denisov,[12] A. Deshpande,[32] E. J. Desmond,[3] O. Dietzsch,[33] B. V. Dinesh,[2] A. Drees,[28] A. Durum,[12] D. Dutta,[2] K. Ebisu,[24] Y. V. Efremenko,[29] K. El Chenawi,[40] H. En'yo,[17,31] S. Esumi,[39] L. Ewell,[3] T. Ferdousi,[5] D. E. Fields,[25] S. L. Fokin,[16] Z. Fraenkel,[42] A. Franz,[3] A. D. Frawley,[9] S.-Y. Fung,[5] S. Garpman,[20] T. K. Ghosh,[40] A. Glenn,[36] A. L. Godoi,[33] Y. Goto,[32] S. V. Greene,[40] M. Grosse Perdekamp,[32] S. K. Gupta,[2] W. Guryn,[3] H.-Å. Gustafsson,[20] J. S. Haggerty,[3] H. Hamagaki,[7] A. G. Hansen,[19] H. Hara,[24] E. P. Hartouni,[18] R. Hayano,[38] N. Hayashi,[31] X. He,[10] T. K. Hemmick,[28] J. M. Heuser,[28] M. Hibino,[41] J. C. Hill,[13] D. S. Ho,[43] K. Homma,[11] B. Hong,[15] A. Hoover,[26] T. Ichihara,[31,32] K. Imai,[17,31] M. S. Ippolitov,[16] M. Ishihara,[31,32] B. V. Jacak,[28,32] W. Y. Jang,[15] J. Jia,[28] B. M. Johnson,[3] S. C. Johnson,[18,28] K. S. Joo,[23] S. Kametani,[41] J. H. Kang,[43] M. Kann,[30] S. S. Kapoor,[2] S. Kelly,[8] B. Khachaturov,[42] A. Khanzadeev,[30] J. Kikuchi,[41] D. J. Kim,[43] H. J. Kim,[43] S. Y. Kim,[43] Y. G. Kim,[43] W. W. Kinnison,[19] E. Kistenev,[3] A. Kiyomichi,[39] C. Klein-Boesing,[22] S. Klinksiek,[25] L. Kochenda,[30] V. Kochetkov,[12] D. Koehler,[25] T. Kohama,[11] D. Kotchetkov,[5] A. Kozlov,[42] P. J. Kroon,[3] K. Kurita,[31,32] M. J. Kweon,[15] Y. Kwon,[43] G. S. Kyle,[26] R. Lacey,[27] J. G. Lajoie,[13] J. Lauret,[27] A. Lebedev,[13,16] D. M. Lee,[19] M. J. Leitch,[19] X. H. Li,[5] Z. Li,[6,31] D. J. Lim,[43] M. X. Liu,[19] X. Liu,[6] Z. Liu,[6] C. F. Maguire,[40] J. Mahon,[3] Y. I. Makdisi,[3] V. I. Manko,[16] Y. Mao,[6,31] S. K. Mark,[21] S. Markacs,[8] G. Martinez,[34] M. D. Marx,[28] A. Masaike,[17] F. Matathias,[28] T. Matsumoto,[7,41] P. L. McGaughey,[19] E. Melnikov,[12] M. Merschmeyer,[22] F. Messer,[28] M. Messer,[3] Y. Miake,[39] T. E. Miller,[40]

A. Milov,[42] S. Mioduszewski,[3,36] R. E. Mischke,[19] G. C. Mishra,[10] J. T. Mitchell,[3] A. K. Mohanty,[2] D. P. Morrison,[3] J. M. Moss,[19] F. Mühlbacher,[28] M. Muniruzzaman,[5] J. Murata,[31] S. Nagamiya,[14] Y. Nagasaka,[24] J. L. Nagle,[8] Y. Nakada,[17] B. K. Nandi,[5] J. Newby,[36] L. Nikkinen,[21] P. Nilsson,[20] S. Nishimura,[7] A. S. Nyanin,[16] J. Nystrand,[20] E. O'Brien,[3] C. A. Ogilvie,[13] H. Ohnishi,[3,11] I. D. Ojha,[4,40] M. Ono,[39] V. Onuchin,[12] A. Oskarsson,[20] L. Österman,[20] I. Otterlund,[20] K. Oyama,[7,38] L. Paffrath,[3,*] A. P. T. Palounek,[19] V. S. Pantuev,[28] V. Papavassiliou,[26] S. F. Pate,[26] T. Peitzmann,[22] A. N. Petridis,[13] C. Pinkenburg,[3,27] R. P. Pisani,[3] P. Pitukhin,[12] F. Plasil,[29] M. Pollack,[28,36] K. Pope,[36] M. L. Purschke,[3] I. Ravinovich,[42] K. F. Read,[29,36] K. Reygers,[22] V. Riabov,[30,35] Y. Riabov,[30] M. Rosati,[13] A. A. Rose,[40] S. S. Ryu,[43] N. Saito,[31,32] A. Sakaguchi,[11] T. Sakaguchi,[7,41] H. Sako,[39] T. Sakuma,[31,37] V. Samsonov,[30] T. C. Sangster,[18] R. Santo,[22] H. D. Sato,[17,31] S. Sato,[39] S. Sawada,[14] B. R. Schlei,[19] Y. Schutz,[34] V. Semenov,[12] R. Seto,[5] T. K. Shea,[3] I. Shein,[12] T.-A. Shibata,[31,37] K. Shigaki,[14] T. Shiina,[19] Y. H. Shin,[43] I. G. Sibiriak,[16] D. Silvermyr,[20] K. S. Sim,[15] J. Simon-Gillo,[19] C. P. Singh,[4] V. Singh,[4] M. Sivertz,[3] A. Soldatov,[12] R. A. Soltz,[18] S. Sorensen,[29,36] P. W. Stankus,[29] N. Starinsky,[21] P. Steinberg,[8] E. Stenlund,[20] A. Ster,[44] S. P. Stoll,[3] M. Sugioka,[31,37] T. Sugitate,[11] J. P. Sullivan,[19] Y. Sumi,[11] Z. Sun,[6] M. Suzuki,[39] E. M. Takagui,[33] A. Taketani,[31] M. Tamai,[41] K. H. Tanaka,[14] Y. Tanaka,[24] E. Taniguchi,[31,37] M. J. Tannenbaum,[3] J. Thomas,[28] J. H. Thomas,[18] T. L. Thomas,[25] W. Tian,[6,36] J. Tojo,[17,31] H. Torii,[17,31] R. S. Towell,[19] I. Tserruya,[42] H. Tsuruoka,[39] A. A. Tsvetkov,[16] S. K. Tuli,[4] H. Tydesjö,[20] N. Tyurin,[12] T. Ushiroda,[24] H. W. van Hecke,[19] C. Velissaris,[26] J. Velkovska,[28] M. Velkovsky,[28] A. A. Vinogradov,[16] M. A. Volkov,[16] A. Vorobyov,[30] E. Vznuzdaev,[30] H. Wang,[5] Y. Watanabe,[31,32] S. N. White,[3] C. Witzig,[3] F. K. Wohn,[13] C. L. Woody,[3] W. Xie,[5,42] K. Yagi,[39] S. Yokkaichi,[31] G. R. Young,[29] I. E. Yushmanov,[16] W. A. Zajc,[8] Z. Zhang,[28] and S. Zhou[6]

(PHENIX Collaboration)

[1]Institute of Physics, Academia Sinica, Taipei 11529, Taiwan
[2]Bhabha Atomic Research Centre, Bombay 400 085, India
[3]Brookhaven National Laboratory, Upton, NY 11973-5000, USA
[4]Department of Physics, Banaras Hindu University, Varanasi 221005, India
[5]University of California - Riverside, Riverside, CA 92521, USA
[6]China Institute of Atomic Energy (CIAE), Beijing, People's Republic of China
[7]Center for Nuclear Study, Graduate School of Science, University of Tokyo, 7-3-1 Hongo, Bunkyo, Tokyo 113-0033, Japan
[8]Columbia University, New York, NY 10027 and Nevis Laboratories, Irvington, NY 10533, USA
[9]Florida State University, Tallahassee, FL 32306, USA

[10]Georgia State University, Atlanta, GA 30303, USA

[11]Hiroshima University, Kagamiyama, Higashi-Hiroshima 739-8526, Japan

[12]Institute for High Energy Physics (IHEP), Protvino, Russia

[13]Iowa State University, Ames, IA 50011, USA

[14]KEK, High Energy Accelerator Research Organization, Tsukuba-shi, Ibaraki-ken 305-0801, Japan

[15]Korea University, Seoul, 136-701, Korea

[16]Russian Research Center "Kurchatov Institute", Moscow, Russia

[17]Kyoto University, Kyoto 606, Japan

[18]Lawrence Livermore National Laboratory, Livermore, CA 94550, USA

[19]Los Alamos National Laboratory, Los Alamos, NM 87545, USA

[20]Department of Physics, Lund University, Box 118, SE-221 00 Lund, Sweden

[21]McGill University, Montreal, Quebec H3A 2T8, Canada

[22]Institut für Kernphysik, University of Münster, D-48149 Münster, Germany

[23]Myongji University, Yongin, Kyonggido 449-728, Korea

[24]Nagasaki Institute of Applied Science, Nagasaki-shi, Nagasaki 851-0193, Japan

[25]University of New Mexico, Albuquerque, NM 87131, USA

[26]New Mexico State University, Las Cruces, NM 88003, USA

[27]Chemistry Department, State University of New York - Stony Brook, Stony Brook, NY 11794, USA

[28]Department of Physics and Astronomy, State University of New York - Stony Brook, Stony Brook, NY 11794, USA

[29]Oak Ridge National Laboratory, Oak Ridge, TN 37831, USA

[30]PNPI, Petersburg Nuclear Physics Institute, Gatchina, Russia

[31]RIKEN (The Institute of Physical and Chemical Research), Wako, Saitama 351-0198, JAPAN

[32]RIKEN BNL Research Center, Brookhaven National Laboratory, Upton, NY 11973-5000, USA

[33]Universidade de São Paulo, Instituto de Física, Caixa Postal 66318, São Paulo CEP05315-970, Brazil

[34]SUBATECH (Ecole des Mines de Nantes, IN2P3/CNRS, Universite de Nantes) BP 20722 - 44307, Nantes-cedex 3, France

[35]St. Petersburg State Technical University, St. Petersburg, Russia

[36]University of Tennessee, Knoxville, TN 37996, USA

[37]Department of Physics, Tokyo Institute of Technology, Tokyo, 152-8551, Japan

[38]University of Tokyo, Tokyo, Japan

[39]Institute of Physics, University of Tsukuba, Tsukuba, Ibaraki 305, Japan

[40]Vanderbilt University, Nashville, TN 37235, USA

[41]Waseda University, Advanced Research Institute for Science and Engineering, 17 Kikui-cho, Shinjuku-ku, Tokyo 162-0044, Japan

[42]Weizmann Institute, Rehovot 76100, Israel

[43]Yonsei University, IPAP, Seoul 120-749, Korea

[44]KFKI Research Institute for Particle and Nuclear Physics (RMKI), Budapest, Hungary[†]

Bibliography

[1] A.M.Poskanzer and S.Voloshin, Phys.Rev.C58(1998)1671.

[2] J.Barrette *et al.*(E877 Collaboration), Phys.Rev.C56(1997)3254.

[3] C.A.Ogilvie,(E802,E806,E917 Collaborations), Nucl.Phys.A630(1998)571c.

[4] H.Appelshauser *et al.*(NA49 Collaboration), Phys.Rev.Lett.80(1998)4136.

[5] A.M.Poskanzer and S.A.Voloshin *et al.*(NA49 Collaboration),
    nucl-ex/9906013.

[6] M.M.Aggarwal *et al.*(WA98 Collaboration), nucl-ex/9807004.

[7] L.P.Csernai and D.Rohrich, Phys.Lett.B458(1999)454.

[8] S.Nishimura *et al.*(WA98 Collaboration), Nucl.Phys.A661(1999)464c

[9] K.Enosawa, Ph.D.thesis, *Study of the Azimuthallly Anisotropic Emission of
    Kaon in 158 A GeV Pb+Pb Collisions at CERN-SPS*,
    University of Tsukuba,1999.

[10] STAR Collaboration (K.H.Ackermann *et al.*), Phys.Rev.Lett.86,402(2001)

[11] STAR Collaboration (K.H.Ackermann *et al.*), Phys.Rev.Lett.87(2001)

[12] PHOBOS Collaboration (Inkyu C. Park *et al.*), Nucl.Phys.A698:564-567(2002)

[13] PHENIX Collaboration (Roy A. Lacey *et al.*), Nucl.Phys.A698:559-563(2002)

[14] J.M.Burward-Hoy, Ph.D.thesis, *Transverse Momentum Distributions of
    Hadrons Produced in Au+Au Collisions at 130 GeV Measured by the PHENIX
    Experiment at RHIC BNL*,
    State University of New York at Stony Brook,2001.

[15] T.Chujo,H.Ohnishi,R.Averbeck,J.Burward-Hoy,A.Drees,F.Messer,
      F.Muehlbacher,J.Velkovska,A.Kiyomichi,
      PHENIX Analysis Note No.37(2001)

[16] M.Ono,M.Shindo,S.Esumi,Y.Miake, PHENIX Analysis Note No.72(2001)

[17] M.Ono,S.Esumi,Y.Miake, PHENIX Analysis Note No.88(2001)

[18] M.Shindo, Graduation thesis(2001)

[19] J.Hill, Draft of PHENIX NIM Articles.

[20] Y.Miake, *Review of High Energy Heavy Ion Experiments*,
      Institute of Physics, University of Tsukuba, 1999.

[21] T.Chujo, Ph.D.thesis, *Study of Single Particle Spectra and Two Particle Cor-
      relations in Au+Au Collisions at 4-11 A GeV*,
      University of Tsukuba,2000.

[22] T.Hachiya, Master thesis(2001)

[23] P.Huovinen,P.F.Kolb,U.Heinz,P.V.Ruuakanen and S.Voloshin,
      Phys.Lett.B503,58(2001)